npj | spintronics

Review

https://doi.org/10.1038/s44306-025-00122-y

Strain-decoupled magnetism in flexible spintronic sensors

Minsun Oh, Yubin Kim & Minjeong Ha ✉

Flexible spintronic sensors provide contactless, vector-resolved readout for wearables, implantable bioelectronics, and microrobotics, yet strain-induced inverse magnetostriction disrupts anisotropy and compromises stability. Magnetoelasticity originates from spin–orbit coupling, orbital hybridization, and exchange interaction in ferromagnets, further intensified by nanoscale thin-films. Strain-decoupled strategies—low-magnetostriction alloys and stress-relaxation architectures—stabilize domain states and preserve sensitivity. Looking forward, multiscale predictive frameworks bridging electronic structure, micromagnetics, and finite-element mechanics offer robust design of strain-resilient, conformable devices.

Flexible spintronic sensors are emerging as key components in next-generation soft electronics and human–machine interfaces. Magnetic field sensing enables contactless[1–4] and proximity-based monitoring of position[5–7], structural transformation[8,9], and spatiotemporally complex motion patterns[9] across a variety of deformable platforms[7–10]. Conventional electromechanical transducers—piezoresistive, capacitive, piezoelectric, triboelectric, mechano-ionic, or optomechanical—necessitate intimate physical contact and often suffer from poor signal stability and signal interference under dynamic loading[10,11]. Distinct from these limitations, spintronic sensors transduce mechanical stimuli into spatially resolved variations in magnetic field magnitude and orientation[4,12–15]. This indirect sensing modality permits high-resolution detection of subtle temporal variations even in unstructured[2,3], visually occluded[12], or geometrically intricate environments[7,13]. These capabilities originate from the intrinsic physics of spintronics, where spin-polarized electron transport and magnetization behavior can be precisely modulated through nanoscale material design and device-architecture engineering[16,17]. Such spintronic devices based on mechanisms including anisotropic magnetoresistance (AMR)[18–21], giant magnetoresistance (GMR)[22–29], tunneling magnetoresistance (TMR)[30–32], Hall effect[33–36], and magnetoelastic coupling[37,38] have been integrated onto soft and ultra-thin substrates to establish mechanically resilient yet flexible platform, allowing the realization of compliant magnetic sensors. These flexible and highly compliant magnetic sensors conform to curved or stretchable surfaces and preserve performance under dynamic conditions[11,12]. This mechanical compliance and functional adaptability broaden the applicability of these sensors, including electronic skin (e-skin) compasses[39], wearable health monitors[40], implantable bioelectronics[21], soft robotic proprioception[9,41], and immersive augmented or virtual reality (AR/VR) systems[22,29].

Flexible spintronic sensors are primarily designed to withstand bending curvature and axial strain while maintaining both magnetic and electrical stability. Despite significant progress, their performance remains limited by sensitivity to mechanical strain, which modifies magnetic anisotropy through inverse magnetostriction (Fig. 1). In this phenomenon, even modest deformation can reorient the magnetization by altering the total magnetic anisotropy energy associated with magnetic domain properties[28,37,38,42–45]. Such unintended strain-magnetism coupling leads to signal drift and degrades the selectivity and precision of magnetic field sensing[15,19,46–48]. These instabilities arise not only under repeated or large-scale deformation but also from subtle variations in strain amplitude or direction, both of which hinder consistent field-sensing performance in mechanically disturbed conditions[7,49–51]. To address these challenges, recent efforts focus on engineering strain-decoupled magnetic responses, in which magnetic field sensitivity is maintained regardless of mechanical loading and deformation[18,21,26,30,52]. Reported strategies include material-level tuning of magnetostriction constants[52–55], implementing magnetostrictive/non-magnetostrictive bilayer stacks to stabilize magnetic anisotropy[21,55], and designing device architectures to redistribute mechanical stress away from active sensing regions[20,29]. At the nanoscale, engineered thin-film architecture and controlled spin–orbit interactions suppress strain-induced reorientation, thereby improving sensitivity and operational reliability[12,39]. In this review, we trace the fundamental origins of magnetoelastic coupling, describe mechanisms of strain-induced magnetic instabilities in nanoscale systems, and highlight emerging design principles for strain-decoupled spintronic sensors. Together, these insights provide a roadmap for high-performance flexible spintronic sensors capable of reliable operation in complex, dynamically deforming environments.

Department of Materials Science and Engineering, Gwangju Institute of Science and Technology (GIST), Gwangju, 61005, Republic of Korea.
✉e-mail: minjeongha@gist.ac.kr

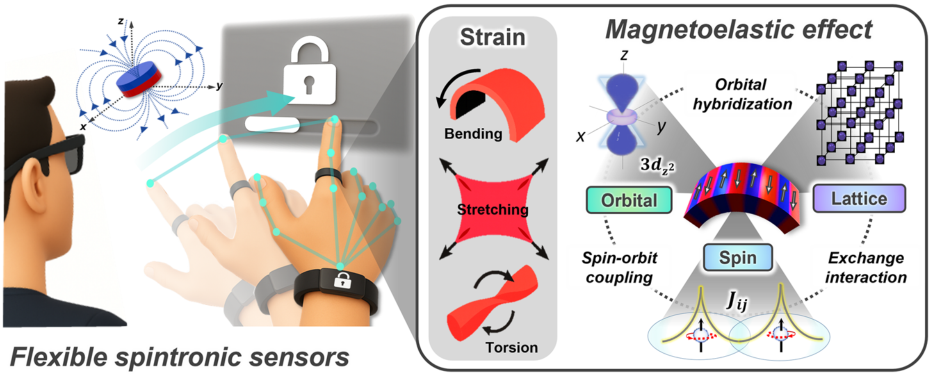

Fig. 1 | Flexible spintronic sensors and strain-induced magnetoelastic coupling. Schematic illustration of flexible spintronic sensors enabling gesture recognition and contactless interaction. Mechanical strain from bending, stretching, or torsion modulates magnetic anisotropy through inverse magnetostriction, originating from orbital hybridization, spin–orbit coupling, and exchange interactions.

Fundamentals of magnetoelastic effect

The magnetoelastic effect describes changes in the magnetic properties of a material in response to mechanical stress through strain-induced modulation of magnetic anisotropy (Fig. 2a)[56,57]. Instead of arising from a single mechanism, it reflects the interplay among spin–orbit coupling (SOC), orbital hybridization, and exchange interactions, each strongly dependent on interatomic distance, as described in Fig. 1[57,58]. SOC-mediated changes in orbital occupation and energy levels under strain provide the microscopic basis for both magnetostriction and its inverse form[59,60]. In inverse magnetostriction, ferromagnets exhibit an intrinsic tendency to reorient magnetization or reconfigure magnetic domains under mechanical deformation[19,42,50,51,61]. This behavior arises from stress-induced variations in anisotropy energy, which shift the balance of competing terms and drive the system into a new magnetization state that minimizes total energy, even if deviating from the initial easy axis[28,62,63]. Thus, despite optimization for high sensitivity and well-defined zero-field reference, the engineered magnetization state in thin-film spintronic sensors is still destabilized by strain-mediated anisotropy fluctuations[16,64]. The total magnetic anisotropy energy is

$$E_{\text{total}} = E_{\text{crys}} + E_{\text{sh}} + E_{\text{ex}} + E_{\text{Zeeman}} + E_{\text{me}} \tag{1}$$

Here, E_{crys} denotes magnetocrystalline anisotropy determined by lattice structure[65,66], E_{sh} is the shape anisotropy governed by the geometry and demagnetizing fields[67,68], E_{ex} represents exchange energy associated with spin-spin interactions, including the exchange strength in bulk ferromagnets or the interfacial exchange anisotropy in multilayered magnetic systems[69,70], E_{Zeeman} is the interaction with the external field (H_{ext})[71,72], and E_{me} is the magnetoelastic energy[73,74]. In strain-mediated systems, E_{me} becomes a dominant and is given by

$$E_{\text{me}} = K_\sigma \sin^2\theta, \tag{2}$$

$$K_\sigma = \frac{3}{2}\lambda_s\sigma \tag{3}$$

where λ_s is the saturation magnetostriction coefficient (dimensionless, typically reported in ppm), σ is the applied uniaxial stress, θ is the angle between magnetization and the stress axis and K_σ is the magnetoelastic anisotropy constant. The sign and magnitude of λ_s determine the preferential orientation of the stress-induced magnetic easy-axis[75,76]:

$$\text{Preferred orientation} = \begin{cases} \parallel \text{ stress axis} & \lambda_s \cdot \sigma > 0 \\ \perp \text{ stress axis} & \lambda_s \cdot \sigma < 0 \\ \text{no stress} - \text{induced anisotropy} & \lambda_s \cdot \sigma = 0 \end{cases} \tag{4}$$

Here, $\sigma > 0$ denotes tensile stress and $\sigma < 0$ denotes compressive stress. Thus, even the same material can exhibit opposite domain reorientations under tensile versus compressive loading. This principle guides sensor design toward two distinct approaches: exploiting specific combinations of λ_s and applied stress σ to achieve desired magnetic responses, or alternatively, isolating the magnetic layers from strain-sensitive regions to minimize the influence from strain. For example, in polycrystalline Permalloy ($Ni_{78}Fe_{22}$, $\lambda_s > 0$), Singh et al. observed that tensile (roll-down) and compressive (roll-up) bending reversed the strain-induced uniaxial anisotropy, reorienting domains accordingly (Fig. 2b)[19]. In AMR measurements, induced azimuthal anisotropy suppressed axial magnetization at zero field, modifying magnetic-field sensing characteristics (Fig. 2c, d). Kong et al. investigated the inverse magnetostriction in single-crystalline Ni lamellae ($\lambda_{110} = -31 \times 10^{-6}$). Under 0.05% tensile strain, the magnetization rotated perpendicular to the strain axis, whereas 0.20% strain reduced the domain-wall width from 75 nm to 43 nm and enhanced the associated stray fields (Fig. 2e)[42]. Micromagnetic simulations reproduced the reorientation and the wall narrowing by revealing reduced three-dimensional (3D) wall twisting (Fig. 2f), directly evidencing strain-controlled magnetization reconfiguration (Fig. 2g).

At the electronic scale, SOC couples spin states to local lattice symmetry, while strain-sensitive exchange interactions and orbital hybridization modifications determine both the magnitude and the sign of the magnetoelastic response (Fig. 3a, b). In $3d$ transition metal systems such as Fe, Co, Ni, and their alloys (e.g., Cu–Ni, Fe–Co)[77], magnetoelastic response is governed primarily by second-order SOC and intra-atomic exchange[57], which in turn mediate strain-dependent variations in magnetic anisotropy and coercivity[78]. Theoretical models, including those by Berger, attribute the sign reversal of λ_s observed in Fe–Ni and Co–Ni alloys to SOC-induced lifting of orbital degeneracy near the Fermi level (Fig. 3c, d)[77]. Mechanical strain shifts orbital degeneracies, leading to competing contributions to λ_s. In contrast, rare-earth elements like Tb^{3+} and Dy^{3+} exhibit significant magnetostriction owing to the localized nature of their $4f$ electrons and the associated strong SOC[79]. Strong SOC fixes the spin and orbital moments into discrete energy levels that are split by the crystal field from the surrounding ions[80]. When $k_bT \ll \Delta_{cf}$, localized $4f$ states preserve significant orbital contribution that couples strongly to lattice distortions[81], thereby amplifying magnetoelastic interactions far beyond those observed in $3d$ transition metals. When system energy is insufficient to overcome crystal field splitting, $4f$ electrons occupy anisotropic orbitals that couple strongly to the lattice, yielding large magnetostriction (Fig. 3e)[82]. The strength of this coupling depends on the Stevens coefficients[58], which parameterize the orbital symmetry across the lanthanide series[83]. Also, ions such as Gd^{3+} or Eu^{2+} have quenched orbital angular momentum[84,85]. In these cases, magnetostriction arises from exchange striction. When sublattice distortions arise below the Néel temperature (T_N), they act to lower the exchange energy (Fig. 3f, g)[86,87]. Although this behavior is distinct from crystal field effect, it

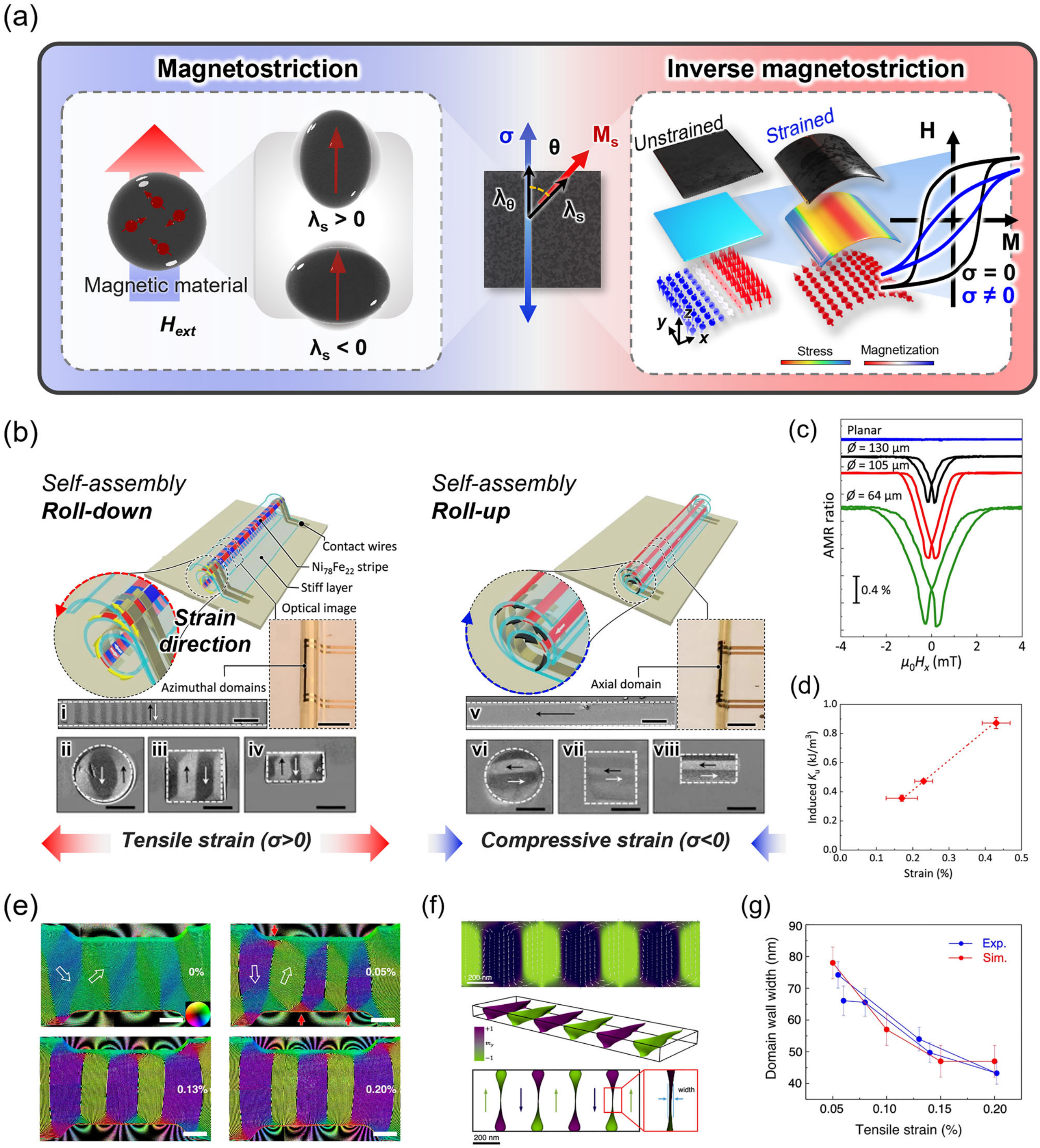

Fig. 2 | Magnetoelastic effect and magnetic anisotropy reshaping. **a** Schematic illustration of the magnetoelastic effect. Depending on the magnetostriction constant (λs), magnetic materials response differently to the coupling between magnetization and applied strain. **b** Roll-down/roll-up self-assembly induces tensile or compressive strain, with domain variances visualized by Kerr microscopy (scale bars: i, v: 200 μm; ii-iv, vi-viii: 15 μm). **c** AMR hysteresis measured in rolled stripes with different curvatures. **d** Azimuthal uniaxial anisotropy estimated from AMR as a function of strain. **b**–**d** Reproduced with permission from ref. 19 Copyright © 2022, Springer Nature. **e** Real-space magnetic induction maps of Ni lamella under tensile strain–release cycles, obtained by off-axis electron holography. Induction directions are indicated by color wheel and arrows; red markers denote flux-closure domains. (scale bars, 0.5 μm). **f** Micromagnetic simulations of Ni under 0.20% strain, showing three-dimensional (3D) domain-wall twisting and wall narrowing with increasing strain. **g** Experimentally measured 180° domain wall width under tensile strain during the second loading cycle compared with micromagnetic simulations. **e**, **g** Reproduced with permission from ref. 42 Copyright © 2023, Springer Nature.

still permits strain-dependent changes in magnetization and is thus relevant to inverse magnetostriction, particularly in antiferromagnetic–ferromagnetic (AFM–FM) hybrid systems[88–90].

Overall, 3*d* transition metal and rare-earth elements highlight that the microscopic origin of magnetoelasticity lies in how strain perturbs the underlying electronic structure. In general terms, mechanical strain influences magnetic anisotropy by modulating SOC[91–93], lifting orbital degeneracy[94–96], and modifying exchange interactions[97–99]. These changes affect both the magnetic anisotropy energy and the equilibrium orientation of magnetization, directly connecting electronic-level variations under

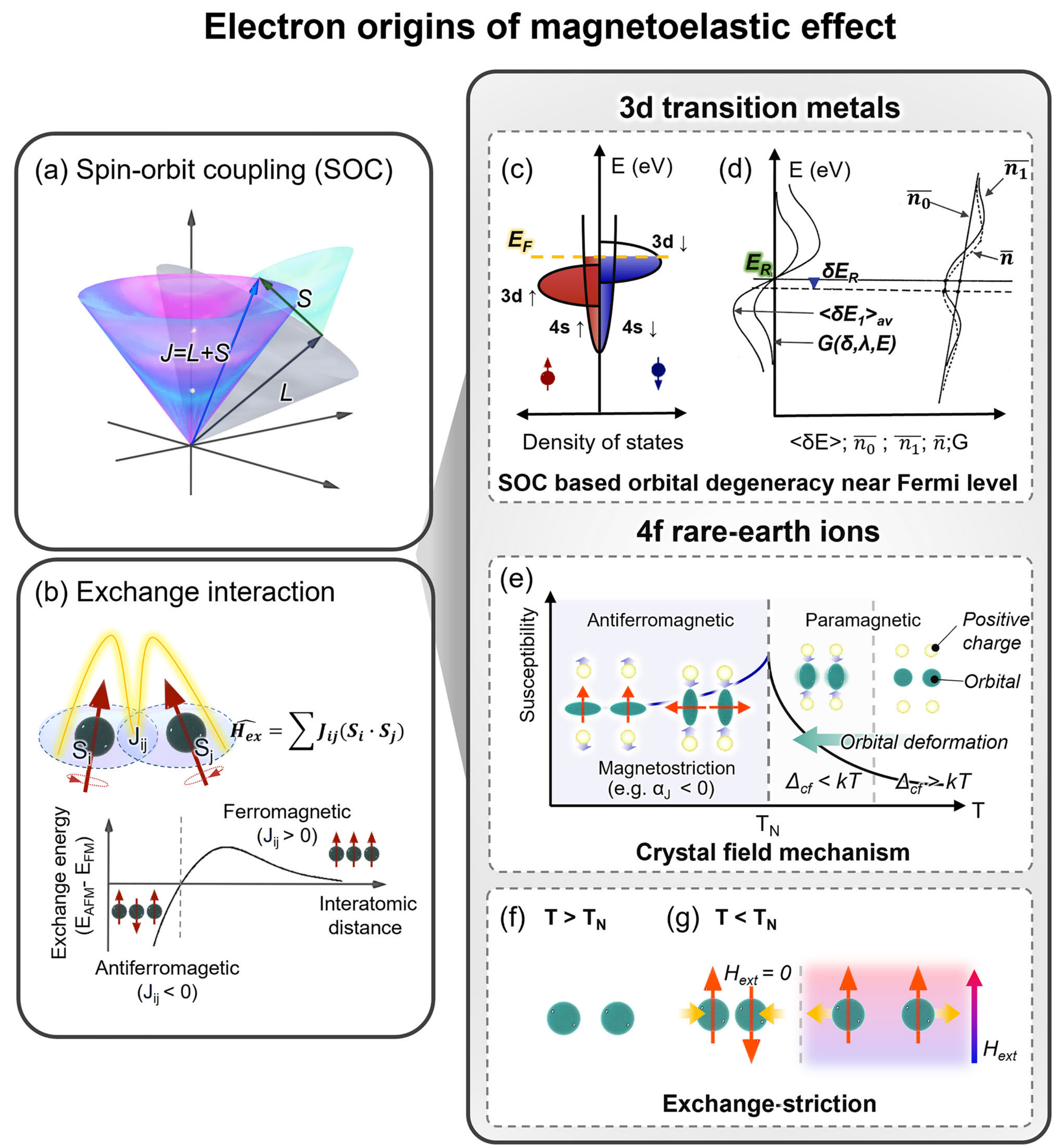

Fig. 3 | Electronic origins of the magnetoelastic effect. a Spin–orbit coupling (SOC). SOC couples orbital (L) and spin (S) angular momentum to the total momentum $J = L + S$, linking orbital symmetry to spin orientation, so that lattice distortions affect magnetic anisotropy. **b** Exchange interaction. The Heisenberg coupling J_{ij} between localized spins S_i and S_j, $J_{ij} > 0$: ferromagnetic alignment, while $J_{ij} < 0$: antiferromagnetic alignment, with magnitude set by interatomic distance. In 3 d transition metals, (**c**) 3d–4s orbital hybridization near the Fermi level. **d** Strain-induced orbital degeneracy shifts the electronic density of states (DOS). The averaged DOS ($\bar{n}$) consists of a baseline ($\bar{n}_0$) and an SOC-strain contribution ($\bar{n}_1$). Degeneracy energy (E_d). Magnetoelastic coefficient (G). As the Fermi level crosses E_d, the magnetostriction constant (λ_s) sign changes. Reproduced with permission from ref. 77 Copyright © 1965, American Physical Society. In 4f rare-earth ions, (**e**) Crystal field mechanism. In rare-earth ions, strong SOC couples spin and orbital moments, while crystal field splitting (Δ_{cf}) determines orbital occupation. Below the Néel temperature ($T < T_N$), anisotropic orbital states couple strongly to the lattice. **f** Paramagnetic phase. When $T > T_N$, thermal energy exceeds crystal field splitting, orbital anisotropy is lost, and magnetostriction becomes negligible. **g** Exchange striction. Below T_N, sublattice distortions lower exchange energy and drive spin reorientation in an external field.

strain to macroscopic magnetoelastic behavior. First-principles insights into these effects advance fundamental understanding of spin–lattice coupling and guide the development of materials with tailored magnetoelastic responses.

Magnetoelasticity in thin-film electronics

In bulk ferromagnetic materials, magnetostriction primarily originates from magnetocrystalline anisotropy, such that λ_s varies sensitively crystal symmetry and structure even at fixed composition[100]. Permalloy

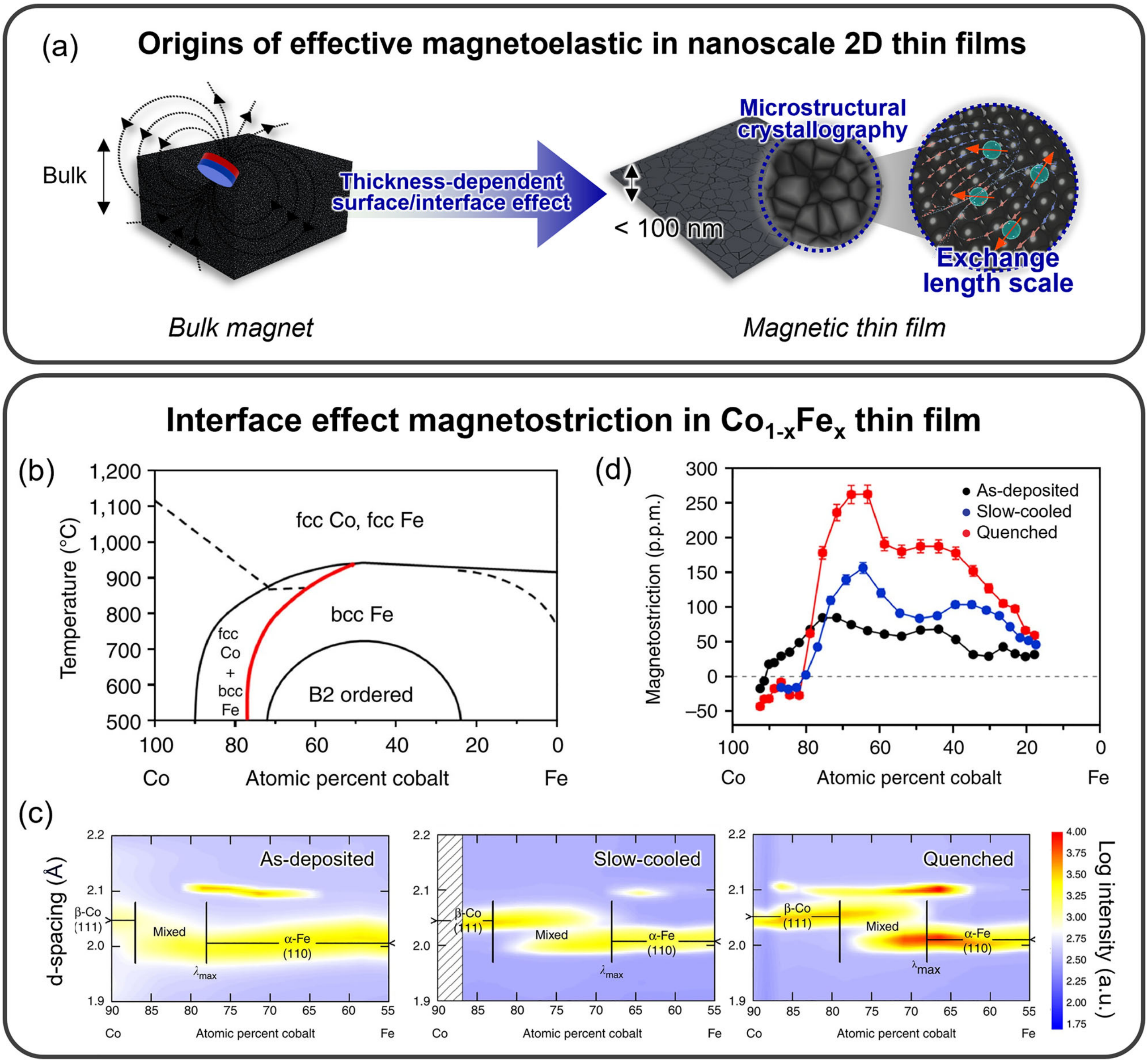

Fig. 4 | Magnetoelasticity in nanoscale magnetic thin-films. **a** Origins of effective magnetoelasticity in magnetic thin-films (λ_s^{eff}). While bulk SOC–lattice coupling dominates in the interior, surface/interface effects and microstructural heterogeneity govern the thin-film response. In polycrystals, the exchange length (L_{ex}) defines the scale over which exchange interaction enforces uniform spin alignment against competing anisotropies. **b** Co–Fe phase diagram highlighting the (fcc + bcc)/bcc boundary coinciding with peak λ_s^{eff}. **c** Synchrotron micro-diffraction revealing thermal-treatment–dependent phase separation from mixed phase in the as-deposited state to Co-rich fcc and Fe-rich bcc phases after quenching. **d** λ_s^{eff} of Co$_{1\text{-}x}$Fe$_x$ films with different interfacial phases. **b**–**d** Reproduced with permission from ref. 192 Copyright © 2011, Springer Nature.

(Ni$_{78}$Fe$_{22}$) exemplifies where the opposing λ_s contributions from Ni and Fe offset each other so that the λ_s approaches zero with a sign reversal near 81% Ni. Ni-rich alloys yield negative λ_s, whereas Fe-rich alloys give positive λ_s, allowing deliberate tuning of composition and stress conditions to approach near-zero magnetostriction[101,102]. However, this compensation diminishes at nanometer-scale thicknesses, where surface-to-volume ratio amplifies surface-specific effects—atomic undercoordination, modified orbital hybridization, and interfacial strain relaxation—dominate the magnetic response (Fig. 4a). As a result, substantial λ_s can emerge otherwise compensated systems, as reported for sub-7 nm Permalloy[103] and in 10-20 nm Fe$_{98}$B$_2$[104], where interfacial strains become the primary contribution. These observations establish dimensional confinement and atomic-scale bonding as decisive parameters for thin-film magnetoelasticity.

To quantify the thickness dependence[105], we begin with the general expression for the local magnetoelastic energy density:

$$E_{\mathrm{me}}(\vec{r}) = -\sum_{i,j} M_{ij}(\vec{r}) \cdot \epsilon_{ij} \tag{5}$$

where $\vec{r}$ is the position vector, M_{ij} is the magnetoelastic tensor, and $\epsilon_{ij}(r)$ is the strain tensor, and i, j are Cartesian tensors indices denoting spatial directions. The negative sign indicates that, for positive λ_s, tensile strain along the magnetization direction reduces the total energy of the system. In thin-film ferromagnets, surface-specific effects modify atomic bonding near interfaces, giving rise to distinct magnetoelastic behavior within surface regions of finite depth (δ), typically corresponding to one to two atomic monolayers. These behaviors can be modeled as interfacial layers with modified magnetoelastic tensors, M_{ij}^{S}, which deviate from their bulk counterparts due to symmetry breaking at the surface and strain relaxation. For a film of thickness, t, and lateral area, A, (volume, V=A t), the total magnetoelastic energy averaged over the film volume is expressed as

$$\bar{E}_{\mathrm{me}} = -\frac{1}{V}\left[\int_{\mathrm{bulk}} \sum_{i,j} M_{ij}^{V}(\vec{r}) \cdot \in_{ij}(\vec{r})\mathrm{d}V) + 2\left(\int_{\mathrm{surf}} \int_{0}^{\delta} \sum_{i,j} M_{ij}^{\mathrm{S}}(\vec{r}) \cdot \in_{ij}(\vec{r})\mathrm{d}z\mathrm{d}S\right)\right] \tag{6}$$

Respectively, $M_{ij}^{V}(\vec{r})$ and $M_{ij}^{\mathrm{S}}(\vec{r})$ denote the bulk and surface components of the magnetoelastic tensor and z denotes the coordinate along the film thickness. Assuming uniform strain and isotropic interface contributions, and noting that both top and bottom surface contribute equally (each with area, A), the expression simplifies to

$$\bar{E}_{\mathrm{me}} = -\sum_{ij} (M_{ij}^{V} + \frac{2\delta}{t} M_{ij}^{\mathrm{S}}) \cdot \epsilon_{ij} \tag{7}$$

Defining the effective surface magnetoelastic tensor, $\widetilde{M}_{ij}^{\mathrm{S}} = \delta \cdot M_{ij}^{\mathrm{S}}$, the thickness-dependent form becomes

$$M_{ij}(t) = M_{ij}^{V} + \frac{2}{t} M_{ij}^{\mathrm{S}} \tag{8}$$

Or in tensor notation:

$$[M] = [M]_{\mathrm{V}} + 2t^{-1}[M]_{\mathrm{S}} \tag{9}$$

This model captures the essential scaling behavior of magnetoelastic interactions in thin films, where surface-specific effects scale as $2/t$ and dominate as $t \rightarrow 0$. The resulting dominance of the contribution of $[M]_{\mathrm{S}}$ leads to pronounced strain sensitivity and anisotropy reshaping widely observed in nanoscale-thickness magnetic thin-films.

Additional complexity is caused by microstructural inhomogeneities near surfaces and interfaces[106–109]. Crystallographic distortions and grain boundary disorder can produce spatial variations in magnetic interactions on length scales smaller than the exchange length, $L_{\mathrm{ex}} = \sqrt{2A/\mu_0 M_{\mathrm{s}}^2}$, where A is the exchange stiffness and M_{s} is the saturation magnetization (Fig. 4a)[110]. For common ferromagnetic materials, L_{ex} is only a few nanometers[111–113], such that grain distortion[114] or crystallographic deformation can directly modify magnetic anisotropy[115] before exchange interactions average out local variations[116]. Building on this concept, Hunter et al. demonstrated that in $\mathrm{Co}_{1\text{-}x}\mathrm{Fe}_x$ thin-films, thermal processing conditions (as-deposited to slow-cooled and quenched states) tune phase coexistence thereby the interfacial environment governing magnetostriction (Fig. 4b). As-deposited films show weak mixed β-Co(111)/α-Fe(110) reflections, whereas slow-cooled films enhance α-Fe near the (fcc + bcc)/bcc phase boundary. Quenched films, in contrast, display clear coexistence of Co-rich fcc precipitates embedded within a Fe-rich bcc matrix (Fig. 4c). Under these quenched conditions, λ_{eff} reaches ~260 ppm near $\mathrm{Co}_{0.66}\mathrm{Fe}_{0.34}$ (Fig. 4d), coinciding with the (fcc + bcc)/bcc phase boundary in the Co–Fe phase diagram (Fig. 4b). These results demonstrate that microstructural heterogeneity and interfacial discontinuities can drive λ_{eff} far beyond bulk values. Extending this principle, microstructural disorder in polycrystalline and amorphous thin-films can drive non-uniform magnetoelastic contributions governed by local bonding environments and magnetic anisotropy. To account for the heterogeneous magnetoelastic response, we introduce an effective thin-film magnetostriction coefficient ($\lambda_{\mathrm{s}}^{\mathrm{eff}}$) as a theoretical parameter describing averaged magnetoelastic behavior in magnetic thin-films:

$$\lambda_{\mathrm{s}}^{\mathrm{eff}}(p) = p\lambda_{\mathrm{s}}^{\mathrm{cr}} + (1-p)\left(\lambda_{\mathrm{s}}^{\mathrm{am}} + kp\right) + \frac{2p}{t}\lambda_{\mathrm{s}}^{\mathrm{S}} \tag{10}$$

Here, $\lambda_{\mathrm{s}}^{\mathrm{cr}}$ denotes the intrinsic magnetostriction of the crystalline phase, weighted by its volume fraction p[117]. Increasing p enhances the nanocrystalline contributions, imposing well-defined easy axes and anisotropy fields[117]. Conversely, the amorphous matrix contributes $(1-p)\left(\lambda_{\mathrm{s}}^{\mathrm{am}} + kp\right)$, where $\lambda_{\mathrm{s}}^{\mathrm{am}}$ represents its inherent magnetostriction and k accounts for progressive reduction of amorphous magnetoelasticity as crystallites grow[117]. This reflects the diminished capacity of the residual amorphous network to sustain uniform spin–lattice coupling. The final term, originally expressed as $p\lambda_{\mathrm{s}}^{\mathrm{S}}(S/V)$[118] is reduced to $\frac{2p}{t}\lambda_{\mathrm{s}}^{\mathrm{S}}$ for thin-films, reflecting the inverse thickness dependence of the surface magnetostriction[105,119]. This interfacial contribution is particularly significant in nanoscale grains, where anisotropy induced by altered surface coordination modifies the local energy and can reorient easy axes relative to the bulk crystalline symmetry. Taken together, the balance among $\lambda_{\mathrm{s}}^{\mathrm{cr}}$, $\lambda_{\mathrm{s}}^{\mathrm{am}}$, and $\lambda_{\mathrm{s}}^{\mathrm{S}}$, modulated by p, dictates whether magnetostriction is governed by crystalline anisotropy, amorphous isotropy, or interfacial discontinuities. These parameters provide a quantitative framework for understanding how microstructure controls local easy axes stability[59], leading to non-uniform magnetization switching even under uniform external stress[120]. From a design perspective, tailoring p, thickness, and interfacial structure enables optimization of effective magnetostriction while maintaining mechanical compliance.

Beyond intrinsic microstructural factors, metallic thin-films experience externally imposed strains. At free surfaces, atomic relaxation contracts the out-of-plane lattice parameter, while growth on substrates with mismatched mechanical properties generates substantial in-plane biaxial strain[121]. This strain arises from thermal-expansion mismatch and lattice distortion, expressed as

$$\eta = \frac{\alpha_s - \alpha_f}{\alpha_s} \tag{11}$$

where η is thermal misfit strain parameter, α_s and α_f are the thermal expansion coefficients of the substrate and integrated metallic thin-film. Such mismatches concentrate residual stress at the film–substrate interface during deposition[122] or transfer[123], leading to misfit dislocations[124] and out-of-plane Poisson-type deformation[125]. Alongside defects originating from deposition and film–substrate integration, additional magnetoelastic effects emerge under applied mechanical loading[126]. Mechanical deformation such as bending, stretching, or torsion induces non-uniform strain at the rigid film-soft substrate interface, resulting in localized lattice distortions (Fig. 5a)[55]. These distortions modify the programmed magnetization direction according to the sign and magnitude of λ_s in the magnetic layers, thereby degrading sensing fidelity—including (i) bias/offset stability, (ii) linearity and hysteresis, and (iii) temporal stability/repeatability—or elevating noise arising from local strain fluctuations that map into an equivalent magnetic-field noise[127]. The extent of this deviation is governed by structural parameters such as film thickness, bending radius, and interfacial adhesion strength at the film-substrate interface[10]. From a mechanical standpoint, the coupled film–substrate system is effectively described by the Stoney equation[128], which relates the biaxial stress σ_f in the film to the substrate curvature ($K = 1/R$) and its elastic properties:

$$\sigma_f = \frac{E_s h_s^2}{6(1-\nu_s)h_f} K \tag{12}$$

where E_s and ν_s are the Young's modulus and Poisson's ratio of the substrate, while h_s and h_f denote the substrate and film thickness. In typical flexible spintronic sensors, with nanometer-thick magnetic layer on a micrometer-thick substrate, the mechanical neutral plane is located within the substrate[129]. Consequently, the magnetic layer undergoes substantial strain and retains residual stress compared to its free-standing state. In heterostructures, stress further localizes at interfaces between dissimilar layers[130], generating interfacial stress gradients that may be obscured in layer-averaged values but nonetheless exert a critical influence on magnetic anisotropy (Fig. 5b).

Furthermore, surface roughness and low interfacial affinity at the film-substrate serve as strain concentrators, amplifying local magnetoelastic

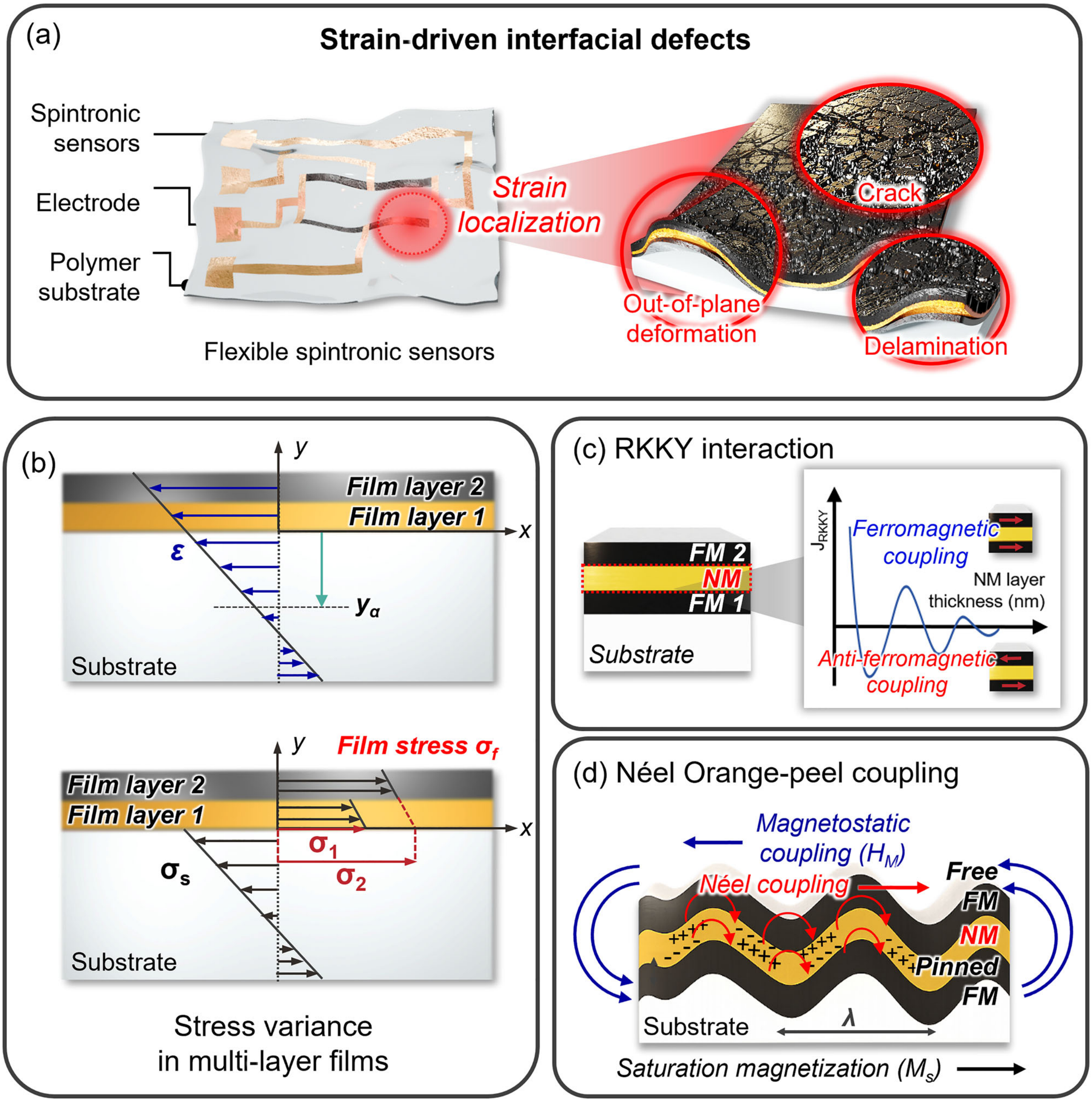

Fig. 5 | Strain and interlayer coupling effects in flexible spintronic thin-films. **a** Strain localization in flexible spintronic sensors induces interfacial defects such as cracks and delamination. **b** Thermal-expansion mismatch and lattice deformation generate stress across multilayers. **c** RKKY interaction. Thickness-dependent indirect exchange coupling mediated by conduction electrons, modulated by strain through spacer thickness changes. **d** Néel orange-peel coupling. Magnetostatic dipolar interaction from interfacial roughness, tuned by tensile or compressive strain. Together these mechanisms explain how strain/stress-induced morphology and deformation govern magnetoelastic responses in multilayer spintronic devices.

coupling. As documented in representative studies, these mechanisms appear consistently across different sensor platforms and loading scenarios. The thickness-dependent indirect exchange interactions such as Ruderman–Kittel–Kasuya–Yosida (RKKY)[131–134] coupling can be modulated by stress, since strain alters spacer thickness and shifts the balance between ferro- and antiferromagnetic alignment (Fig. 5c)[135]. Also, orange-peel coupling, a dipolar interaction originating from interfacial roughness, can be modified by deformation[136]. Tensile strain can suppress coupling by reducing surface asperities, while compressive strain may enhance coupling and promote synchronized switching (Fig. 5d). Although distinct in origin, both mechanisms are governed by stress-induced changes in layer morphology and thickness across the spintronic multilayers, providing additional pathways to tune the effective magnetoelastic response. Under cyclic loading, these effects may further occur initiating mechanical failure such as cracking or delamination[55]. Thus, ensuring magnetic stability under strain requires minimizing unintentional anisotropy modulation—particularly through strain-decoupling approaches—by precisely tuning λ_s^{eff}, controlling grain size and orientation, preserving robust anisotropy, and reducing extrinsic mechanical mismatch—key factors summarized in Table 1, within a design strategy tailored to the target application.

Strain-decoupled flexible spintronic sensors

Strain-decoupled operation in flexible spintronic sensors requires two coordinated strategies. (i) suppressing the intrinsic magnetoelastic

Table 1 | Nanoscale structural factors influencing strain transfer in magnetic materials on flexible substrates

Factor	Physical origin/metric	Effect to magnetic layer	Magnetic impact	Control strategy
Interface Adhesion/ Chemistry	Work of adhesion, interfacial affinity, interlayers	Poor adhesion → stress concentrators, higher local strain (ε) at the interface.	Easy-axis drift[170]; domain pinning[171], $1/f$ noise increase[172].	Adhesion buffer layers (Ti/Cr/Ta)[173], chemical activation[174], 2D/soft buffer to relax mismatch[55,175].
Surface Roughness	RMS/ξ of topography (ξ: correlation length)	Geometric stress amplification, roughness-induced coupling (strain-induced).	Orange-peel coupling[176], H_c increase[177].	Planarization[170], deposition optimization[178], controlled roughness to tune coupling[179].
Grain Boundary (Size d vs L_{ex})	Sub-L_{ex} (Exchange length), heterogeneity, crystallographic disorder.	Non-uniform load paths, local anisotropy variation ΔK.	Barkhausen noise[180], H_c variability[180], inhomogeneous reversal[181].	Annealing[182], texture control[183], nanocrystalline stabilization ($d < L_{ex}$)[110].
Film Texture/Crystallinity	Preferred orientation, Phase coexistence, λ_s	Anisotropic elastic response, λ_s sign/ magnitude shifts.	H_k (anisotropy field) reshaping[184], λ_{eff} deviation from bulk[185].	Seed/templating[186], post-anneal[187], disorder engineering to $\lambda_s \approx 0$[188]
Layer Sequencing / Spacer Thickness	RKKY (long-range exchange) and dipolar roughness coupling.	Stress-modulated coupling, effective thickness and anisotropy.	FM/AFM alignment shifts[189], loop symmetry change (Exchange Bias)[190], H_{eb} modulation[190].	Spacer tuning[167], capping[167], robust pinned/ reference layer design[167].
Neutral-Plane / Buffer Modulus	Stack geometry and modulus mismatch, distance from neutral axis.	Lower surface strain (ϵ_{surf}) when magnetic layer is near neutral plane.	Reduced E_{me} (effective stress)	Thickness balancing[22], compliant buffer layers[191], mesh/serpentine geometry[10].

susceptibility of the sensing layer and (ii) reducing stress propagation through engineered layer design. In the product $\lambda_s \cdot \sigma$ that governs inverse magnetostriction, λ_s is suppressed by compositional and microstructural engineering of magnetic thin-films, whereas σ is minimized by engineering film substrate mechanics to suppress stress propagation. In general, spintronic devices exhibit several dominant noise sources, including thermal noise originating from frequency-independent electron motion[137], flicker noise arising from carrier trapping and detrapping at defects or imperfect interfaces[138,139], shot noise generated at tunneling junctions[140], and magnetic noise caused by domain-wall motion[141] and magnetization nonuniformity[142]. Beyond these intrinsic noise sources, flexible spintronic devices experience additional noise contributions due to their susceptibility to mechanical deformation. Such deformation or processing-induced stress can further destabilize domain rotation[143,144] and electrical contacts[145,146], thereby amplifying low-frequency magnetic noise[147,148]. To clarify this aspect, we introduce a field-referred formulation that quantitatively relates local strain fluctuation to equivalent magnetic-field noise *via* magnetoelastic coupling, positioning strain-induced magnetoelastic noise within the broader framework of intrinsic and extrinsic noise sources. Under mechanically constrained condition, the applied strain ($\varepsilon = \sigma/Y$) produces an effective magnetoelastic field (H_{me})[74]:

$$H_{me} = \frac{2K_\sigma}{\mu_0 M_s} = \frac{3\lambda_s Y}{\mu_0 M_s}\varepsilon \tag{13}$$

This internal field shifts the equilibrium state of magnetization[149], which can be expressed as an equivalent magnetic-field (ΔB_{eq}) offset:

$$\Delta B_{eq} = \mu_0 H_{me} = \frac{3\lambda_s Y}{M_s}\varepsilon \tag{14}$$

The field sensitivity of a magnetic sensor can be generally defined as

$$S_B = \frac{1}{X}\frac{\partial X}{\partial B} \tag{15}$$

where X represents the measurable output quantity—such as resistance (MR sensors)[18], impedance (MI sensors)[150,151], or Hall voltage (Hall devices)[34,152]. Because the output variation under strain follows any change in the ΔB_{eq} directly modulates the apparent sensitivity[152,153]. Thus, an increase in the λ_s or applied ε enlarges ΔB_{eq}, changing the field sensitivity of any spintronic sensing element. In addition, following the formulation of the magnetic-noise power spectral density[154], the strain-induced magnetoelastic contribution to the output-voltage noise can be expressed as

$$S_{V_{out}}^{me}(f) = \left(\frac{\partial V}{\partial B}\right)^2 \left(\frac{3\lambda_s Y}{M_s}\right)^2 \left|H_{mech}(f)\right|^2 S_\varepsilon(f) \tag{16}$$

where $S_\varepsilon(f)$ represents the spectral density of local strain fluctuations and $\left|H_{mech}(f)\right|$ denotes the mechanical transfer function that associates substrate deformation to the magnetic layer. This relationship quantitatively describes how mechanical strain noise is converted into magnetic-field noise and subsequently to output-voltage (V_{out}) fluctuations through the field-to-voltage responsivity ($\partial V/\partial B$) of sensor. It further implies that both material parameters (λ_s, Y, M_s) and structural design factors embedded in $H_{mech}(f)$ govern the overall noise magnitude. Therefore, optimizing the magnetic material for low λ_s and engineering mechanical architectures to suppress strain transmission are essential strategies for minimizing magnetoelastic noise in flexible spintronic sensors.

Compositional and microstructural engineering is directed toward minimizing λ_s^{eff} without compromising the electronic and magnetic functionalities that enable precise and stable spintronic sensor operation. Rivkin et al. demonstrated this approach in self-assembling electroactive-polymer microcatheters incorporating Permalloy-based AMR bridges (Fig. 6a, b)[21]. Field sweeps before and after rolling confirmed stable magnetic field

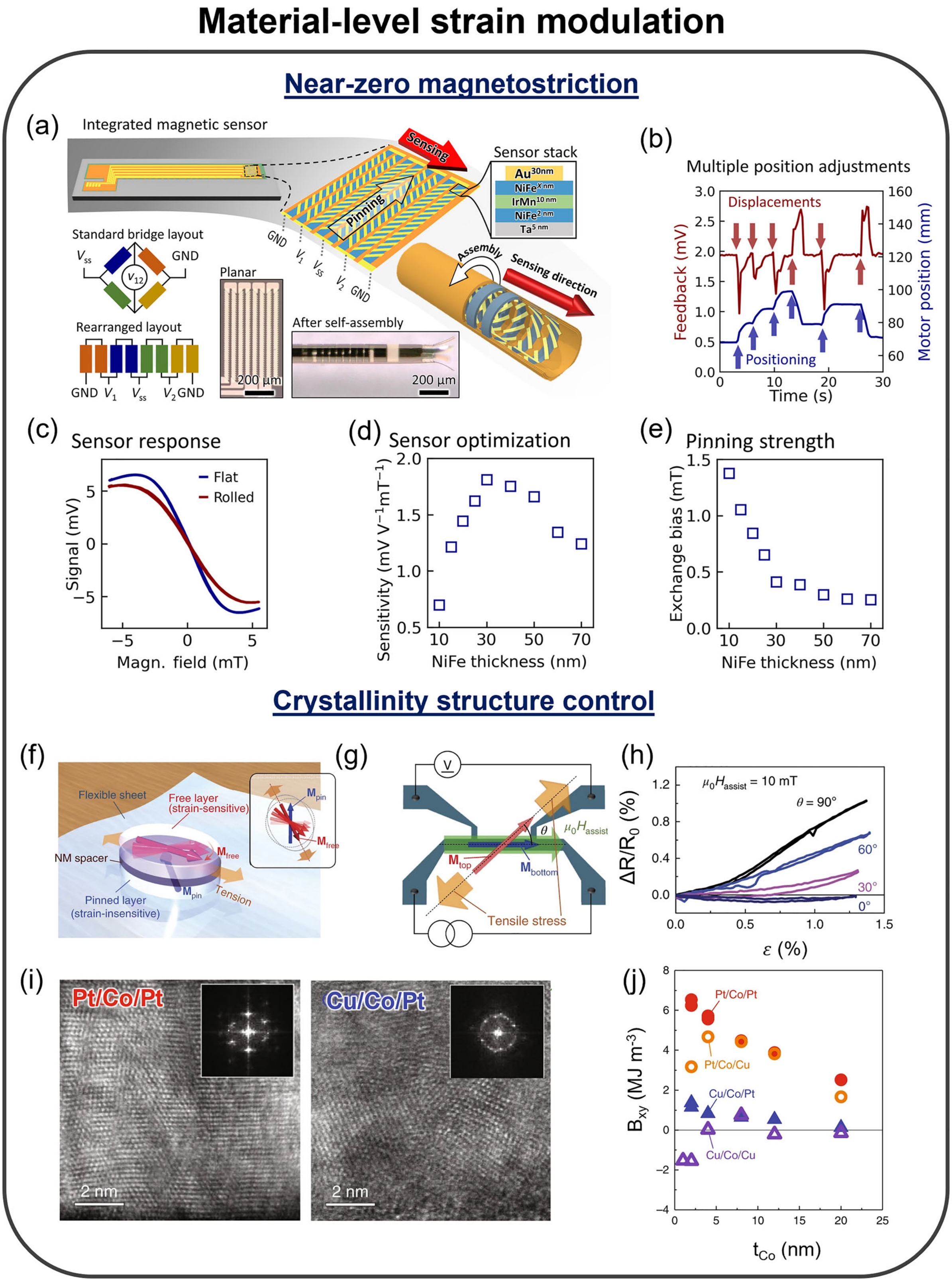

selectivity despite complex 3D deformation (Fig. 6c). This robustness is attributed to the near-zero magnetostriction ($\lambda_s \approx 0$) of 30 nm-thick Permalloy combined with IrMn exchange bias that pins the sensing axis during self-assembly (Fig. 6d, e)[101,103], as demonstrated in flexible spin valves and magnetoelastic tuning of anisotropy under stress[62,63]. The magnetic stripes were patterned orthogonal to the catheter axis, and after rolling to a radius of 0.1 mm, the devices remained sensitive to axial fields along the catheter while suppressed cross-axis response. Minimizing λ_s together with exchange-bias stabilization effectively suppresses stress-driven anisotropy drift. Ota et al. demonstrated a complementary approach in which high-λ_s ferromagnets such as Co can be rendered effectively strain-insensitive through crystallinity-disorder engineering (Fig. 6f)[28]. In a GMR trilayer, the

Fig. 6 | Strain-modulated flexible spintronic sensors *via* material-level engineering. Permalloy-based AMR sensors. **a** Self-assembled AMR microcatheter shown flat and after rolling. Layer stack and rearranged Wheatstone bridge are indicated with optical micrographs. **b** Feedback-controlled positioning by AMR microcatheter. Multiple reference-magnet displacements and corrective motor responses. **c** Field-sweep signal before and after self-assembly (1 V bias). **d** AMR sensor sensitivity versus top NiFe layer thickness. **e** Exchange bias of the AMR stack, measured by Kerr microscopy. **a**–**e** Reproduced by[21] Copyright © 2021, AAAS. Crystal structure designed GMR sensors. **f** Flexible MR device consisting of a strain-sensitive free layer and strain-insensitive pinned layer, separated by a non-magnetic spacer on a flexible substrate. Under tension, only M_{free} rotates toward the stress direction, while M_{pin} remains fixed. **g** Experimental set-up for strain direction sensing (**h**) GMR curves demonstrating strain-insensitive sensing when disordered-Co M_{free} layers are used. **i** Cross-sectional TEM images of Co on Cu (disordered, strain-insensitive) versus Co on Pt (highly crystalline, strain-sensitive). **j** In-plane magnetoelastic constant B_{xy} versus grain structure, showing suppression in Cu/Co/Pt (**f**–**j**). Adapted[28] with permission, Copyright © 2018, Springer Nature.

integration of strain-insensitive and strain-sensitive Co constituents enables directional sensing analogous to differential signal processing (Fig. 6g, h). In Cu/Co/Pt stacks deposited on flexible PEN, the poor crystallinity of the Cu underlayer induced random crystallinity in a 12-nm-thick Co film, resulting in near-zero in-plane magnetoelastic coupling constant (B_{xy}). By contrast, Pt/Co/Pt promotes high crystallinity and a positive B_{xy}, leading to strain sensitivity (Fig. 6i, j). Material-level control of magnetoelastic response supports miniaturization, process versatility, and seamless system integration, yet it cannot fully remove stress concentrations at heterogeneous interfaces or device boundaries.

Geometric factors such as film thickness and bending radius, together with design strategies including multilayer configurations and engineered interfaces, provide complementary pathways to reduce σ by redistributing mechanical load. In thin-film heterostructures, the local strain profile is determined by elastic moduli, curvature, and boundary constraints, and mismatches give rise to heterogeneous stress distributions. To further reduce interfacial stress, compliant geometries or controlled heterogeneity can be introduced, limiting stress transmission to the magnetic layer without compromising electrical continuity. A representative strategy involves pre-stretching and releasing elastomeric substrates, with the elastic modulus mismatch between magnetic thin-films and elastomers providing the driving force for buckled structure formation. Melzer et al. deposited GMR multilayers onto biaxially pre-stretched elastomer substrates[12]. Upon release, the films formed periodic micro-buckles that acted as strain-relief features (Fig. 7a). According to thin-film wrinkling mechanics, such buckling reduces the in-plane strain in the film approximately in proportion to the square of the amplitude-to-wavelength ratio of the wrinkles[155]. Therefore, the buckled devices preserved magnetoresistance performance up to 270% elongations over 1000 cycles and conformed to soap bubbles without rupture (Fig. 7b, c). Open-mesh structures also reduce strain by accommodating deformation within the mesh, thereby preventing stress propagation to the magnetic layer. Makusho et al. patterned GMR thin films into 100 μm-pitch interconnected meshes (Fig. 7d), producing localized strain in conductive lines while allowing open regions to deform freely. Additionally, finite-element analyses confirmed that open-mesh or serpentine geometries accommodate tensile deformation through out-of-plane bending, twisting, and local rotations (Fig. 7e)[29], resulting in an order-of-magnitude reduction in local strain compared to continuous films (Fig. 7f)[129,156,157]. This design enabled large-area field mapping (120 × 120 mm^2) with ~1 mm resolution, optical transparency, and three orders of magnitude lower power consumption than transistor-based matrices, all with skin-conformal integration for VR/AR applications (Fig. 7g).

In addition, soft composite matrices can provide a complementary strategy, encapsulating rigid magnetic layers to decouple them from external stress and strain and thus preserve their functional integrity[10]. Ha et al. suggested embedding GMR micro-flakes within an elastomeric poly(styrene–butadiene–styrene) (SBS) binder and printed them on ultra-thin (3 μm) polymer foils (Fig. 7h)[22]. The viscoelastic SBS binder dissipates mechanical impact through elastic energy storage and time-dependent relaxation[158], thereby protecting the integrity of the composite. Importantly, the large modulus contrast between the soft binder and rigid fillers ensures that the GMR micro-flakes undergo minimal deformation[159] and thus maintain their functional stability. Within the composite, the embedded GMR micro-flakes form a robust percolated network that preserves electrical continuity. With the elastomeric matrix absorbing mechanical stress, the GMR sensors sustained bending down to a 16-μm radius and biaxial strains exceeding 100% (Fig. 7i, j). In parallel, the percolated network of GMR micro-flakes reorganizes without losing connectivity, a feature crucial for stable device performance in skin-mounted gesture-control applications (Fig. 7k).

To offer a comprehensive overview, Table 2 summarizes representative studies that implement strain-decoupling strategies at both the material and device levels in flexible spintronic sensors, emphasizing their performance metrics, fabrication complexity, and potential for large-scale integration. These design strategies highlight that effective strain decoupling is best achieved when intrinsic and extrinsic mechanisms are integrated in a coordinated manner. Material-level suppression minimizes the amplitude of magnetoelastic anisotropy modulation, whereas structural engineering reduces the actual stress propagation to the magnetic layer. In optimized systems, $\partial E_{\mathrm{anisotropy}}/\partial\sigma$ approaches zero, ensuring sensor stability even under severe or cyclic deformation. Looking ahead, predictive multiscale modeling that couples micro-magnetics to finite-element mechanical analysis will enable the systematic tuning of λ_s^{eff}, crystallographic distributions, and stress-propagation or strain-redistributed geometries. Such combined approaches are poised to deliver next-generation flexible spintronic sensors that operate reliably under continuous, multidirectional deformation—unlocking transformative opportunities in soft robotics, bio-integrated navigation, and adaptive human–machine interfaces.

Outlook and future perspectives: toward mechanically resilient, shape-conforming spintronic sensors

This review redefines inverse magnetostriction as a controllable parameter, allowing the tailoring of magnetic field selectivity to improve sensitivity and functional specificity in flexible spintronic devices. Such flexible spintronic sensors encompass systems capable of tolerating gentle bending as well as substantial uniaxial and multiaxial stretching, where mechanical compliance must be precisely engineered to preserve magnetic stability under complex deformation. Reliable magnetic sensing on curved and dynamically deforming platforms becomes feasible when the effective thin-film magnetostriction is reduced through compositional tuning and crystallographic engineering of magnetic thin-films, together with device-level architectures that prevent stress propagation into the active regions. While these material and structural strategies effectively suppress magnetoelastic noise, they inevitably involve trade-offs. Introducing structural buffers improves mechanical resilience but can increase stack thickness and fabrication complexity. Buckled or mesh geometries relieve mechanical stress yet compromise surface planarity and device fill factor. An alternative is algorithmic compensation *via* post-signal processing, which can correct strain-induced artifacts[160]. However, this approach demands large training datasets spanning magnetic-field ranges and deformation states, and leads to longer calibration times and higher on-device power consumption[161,162]. Therefore, achieving an optimal balance among noise suppression, sensitivity preservation, and fabrication practicality in device-level designs remains central to the development of strain-decoupled flexible spintronic sensors.

Magnetic stability in strain-decoupled spintronic sensors can be enhanced by positioning magnetic layers close to the neutral mechanical plane, incorporating reference channels and bias networks to suppress offset drift, and employing island[129] or meta-structured[163] layouts to physically

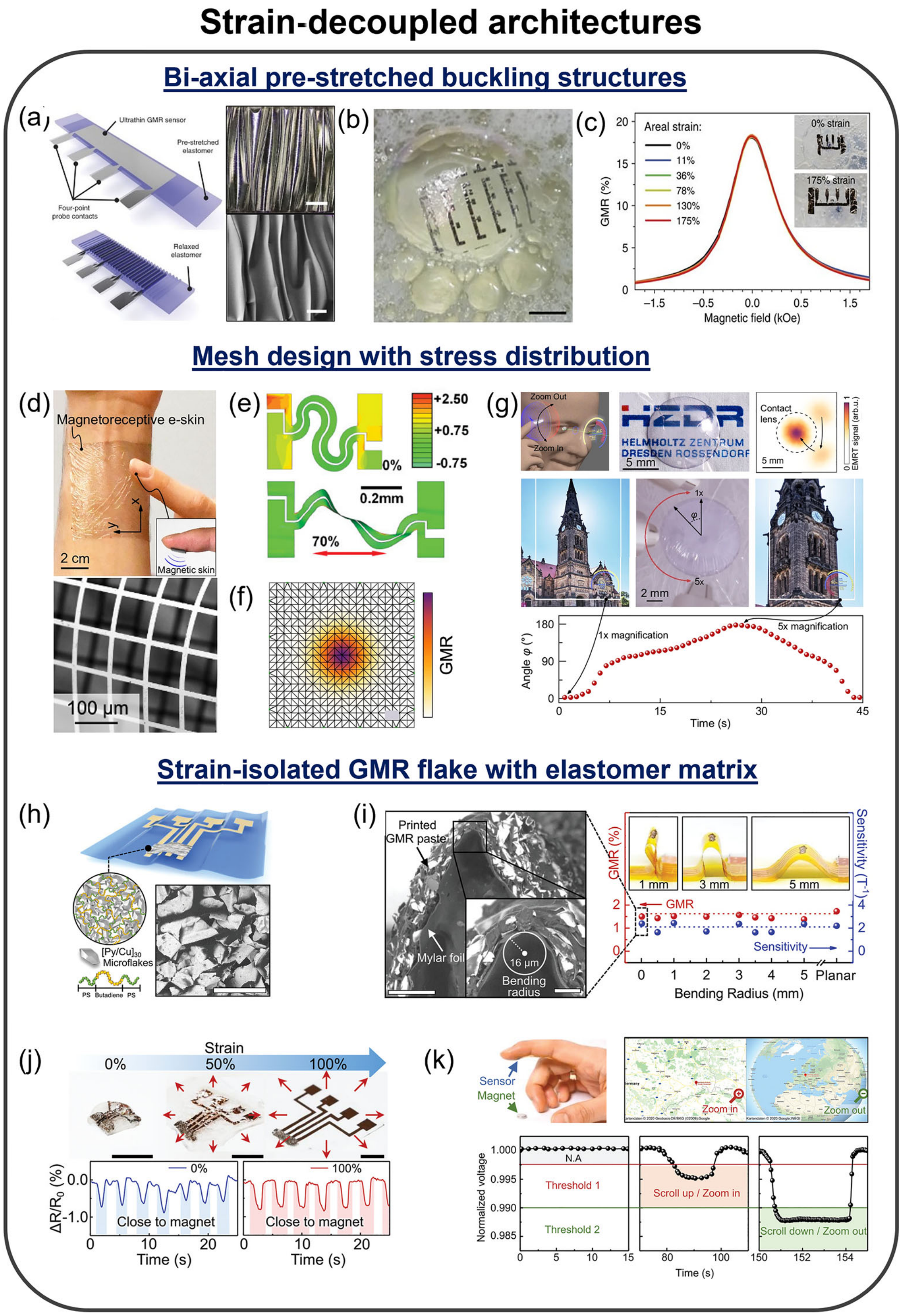

Fig. 7 | Strain-decoupled flexible spintronic sensors *via* structural engineering. Pre-stretched buckling. **a** Top: Schematic of a GMR multilayer on ultrathin PET laminated face-down onto pre-stretched elastomer. Relaxation induces out-of-plane wrinkles that permit subsequent re-stretching. Bottom: Optical (Scale bar, 200 µm) SEM (100 µm) images showing compressed-state wrinkle morphology. **b** Ultralight sensor array floating on a soap bubble. **c** GMR curves under different areal strains are shown; insets display the biaxially wrinkled sensor at 0% and 175% strain. **a**–**c** Adapted by[12], Copyright © 2015, Springer Nature. Mesh-structured sensors. **d** Magnetoreceptive e-skin applied to a human wrist. Inset, NdFeB composite magnetic skin on a fingertip. Right: SEM image of a perforated magnetoreceptive mesh. **e** Finite-element strain maps before (35% pre-strain) and after (70% applied strain) stretching[157], Copyright © 2008, The National Academy of Sciences of the USA. **f** Spatial map of GMR-induced resistivity variation. **g** Concept of magnetically responsive interaction layers enabling virtual interface control *via* electrical magnetoresistive tomography (EMRT). Demonstration with a transparent, compliant contact lens and reconstructed angular tracking. **d**, **f**, **g** Adapted by[29], Copyright © 2025, Springer Nature. Printable GMR composites. **h** Schematic of a printed GMR sensor. $[Py/Cu]_{30}$ micro-flakes dispersed in an SBS tri-block matrix on ultrathin foils. SEM image of dried GMR paste on Mylar (Scale bar: 100 µm). **i** Left: Cross-sectional SEM of a bent device (radius down to 16 µm, inset, and Scale bars: 100 µm, 20 µm, inset). Right: GMR magnitude and sensitivity versus bending radius (Planar to 16 µm). **j** Transition from 100% stretched to relaxed. (Scale bar: 5 mm) Bottom: Time-depenkdent normalized resistance under a moving permanent magnet. **k** Touchless interactive control by sensing finger-magnet distance and mapping to scrolling/zooming functions. **h**–**k** Adapted by[22], Copyright © 2021, Wiley-VCH.

Table 2 | Summary of material-level and device-level strain-decoupling strategies in flexible spintronic sensors

Strain decoupling strategy	Key Strategy/structural feature	Sensor type	Performance	Fabrication complexity	Cost/scalability	Applications	Ref.
Material-level strain modulation	Amorphous CoFeB film with pre-applied stress and magnetic field during deposition	CoFeB film; CoFeB(70 nm)/Ta(3 nm) on PI	Mr/Ms = 0.92 → 0.43 (with pre-strain), 0.77 → 0.14 (without pre-strain)	Low – simple sputtering	Moderate–Low – common CoFeB alloy, limited scalability due to pre-strain setup	Magnetic field sensors, nonvolatile magnetic memories	Qiao et al.[166]
	Crystallinity control with amorphous Cu layer	GMR sensor; Ta(2.5 nm)/Cu(2.0 nm)/Co(4.0 nm)/Cu(4.5 nm)/Co(1.6 nm)/Pt(1.8 nm) on PEN	MR ≈ 1.49%, tunable λs by Co thickness and NM-layer choice	Medium – precise sputtering and interface control	Moderate – uses common 3 d metals (Co, Cu), scalable by sputtering	Flexible strain-direction mapping, e-skin, soft robotics	Ota et al.[28]
	Strong perpendicular magnetic anisotropy (PMA)	PMA multilayer film; Ta(2 nm)/Pt(20 nm)/$[Co(t)/Pt(0.5\ nm)]_4$/Pt(1.5 nm) on PVDF (100 μm)	Mr/Ms > 0.97, robust PMA maintained under in-plane stress ≤ 3.1 GPa	Medium – room-temperature magnetron sputtering	High scalability, moderate cost – wafer-scale compatible (Pt/Co multilayers)	Stress-stable PMA films, flexible spintronic memory and SOT devices	Li et al.[168]
	Low-λs magnetic alloy (NiFe) / Self-assembled rolled-up structure	AMR sensor; Ta(5 nm)/NiFe(2 nm)/IrMn(10 nm)/NiFe(30 nm)/Au(30 nm) on PI	Sensitivity ≈ 1.8 mV mT^{-1} (at 1 V bias), stable up to > 2000 bending cycles	Medium–High – multilayer sputtering and self-assembly	Moderate – wafer-scale batch process (limited by roll-up uniformity)	Flexible AMR sensors for navigation, implantable bioelectronics, microrobots	Rivkin et al.[21]
	Exchange-biased multilayer with low-crystallinity AFM and strong PMA	Exchange-biased multi-layer film; Ta(4 nm)/Pt(2 nm)/IrMn(6 nm)/$[Co(0.6\ nm)/Pt(1\ nm)]_3$/Pt(1 nm) on PI (50 μm)	H_{eb} ≈ 300 Oe (–25% @ 2% strain), $ΔH_{e}b/ε$ ≈ 5.5, remanence > 0.95, elastic ≤ 3% before microcracks	Medium – precise thickness and interface control	Moderate – Pt/IrMn/Co multilayers on flexible substrates	Flexible magnetic sensors, memory devices for wearable electronics	Bao et al.[167]
Strain-decoupling architectures	Pre-strained wrinkled structure	GMR sensor; Co(1 nm)/$[Co(1\ nm)/Cu(1.2\ nm)]_{50}$ on PET (1.4 μm)	MR ≈ 18%, stretchability > 270%, lightweight (~3 g m^{-2}), > 1000 cycles without fatigue	Medium – controlled thin-film thickness and interface precision	Medium–High – low-cost materials, scalable lamination	On-skin magnetosensory systems, soft robotics, wearable electronics	Melzer et al.[12]
	Geometric strain isolation (meander layout + encapsulation)	GMR sensor; Py(1.5 nm)/$Cu(2.3\ nm)]_{30}$ meander pattern on Parylene (1.5 μm)	MR ≈ 10–13%, operational @ 2 mm bending radius, static power 0.8 nW, dynamic power 0.23 μW (100 Hz)	High – lithographic patterning and encapsulation	Medium – limited by patterning throughput	E-skin, magnetic-field mapping	Kondo et al.[23]
	Strain-isolated GMR flakes embedded in elastomer binder	GMR sensor; $[Py(1.5\ nm)/Cu(2.3\ nm)]_{30}$ microflakes in SBS triblock copolymer matrix	MR ≈ 1.5–1.95%, sensitivity ≈ 3 T^{-1}Bending radius ≈ 16 μm, stretchable to 100%, stable up to 90 °C	Low – solution processing and printing	High – roll-to-roll compatible, excellent throughput	On-skin stretchable magnetic sensors, e-textiles	Ha et al.[22]
	Ultrathin delaminated GMR on sub-μm PI buffer	Spin-valve GMR sensor; Ta(5 nm)/Ru(2 nm)/IrMn(8 nm)/CoFe(2 nm)/Ru(0.9 nm)/CoFe(4 nm)/CoFe(3.5 nm)/NiFe(4.5 nm)/Cu(4 nm)/Ru(2 nm) on PI (0.97 μm)	GMR ≈ 2.46%, SNR > 400, bending angle ≤ 90°, > 500 bending cycles	Medium – lift-off and delamination transfer	Medium–High – wafer-to-flex transfer compatible	Flexible e-skin, touchless HMI, biomedical devices	Zhang et al.[24]
	Mesh design with distributed strain	GMR sensor; $[Co(1\ nm)/Cu(2.2\ nm)]_{50}$ bilayer stack on Mylar (2.5 μm)/	MR ≈ 23% (@ ±200 mT), 100% uniaxial strain, > 1000 bending cycles	Medium – multilayer sputtering with precise thickness control	High – scalable polymer process for large-area integration	Touchless HMI, XR/VR/AR interfaces, magnetoreceptive contact lens	Makushko et al.[29]

Note. Fabrication complexity was assessed considering (i) the number of deposition or patterning steps, (ii) the requirement for high-precision alignment or microfabrication, (iii) material composition (use of noble metals, polymers, or adhesives), (iv) processing temperature, and (v) feasibility of large-area integration. “Low” complexity denotes single-step or few-layer fabrication; “Medium” corresponds to multilayer or polymer-assisted architectures requiring moderate control; and “High” involves lithographic or circuit-integrated processing. Cost/scalability reflects the potential for roll-to-roll or polymer-based manufacturing relative to batch-type microfabrication.

isolate active regions. When processing involves high thermal budgets or energetic inputs such as plasma, ion, or laser exposure, the lattice and modulus mismatches between soft supports and magnetic layers are intensified, making direct growth on soft substrates impractical[164]. Thus, by fabricating films or devices on rigid wafers and subsequently transferring them onto soft supports, process compatibility with conventional microfabrication can be preserved[123,165]. However, the release and lamination steps often introduce additional interfacial stress that degrades film integrity and device performance. Minimizing local stress concentrations and improving interfacial adhesion during the transfer process can be achieved through interfacial engineering strategies, such as using adhesion-modifying buffer layers, modulus-matching interlayers, and chemical surface treatments. Ultimately, the mechanical and functional reliability of deformable spintronic systems is enhanced when the active magnetic layers exhibit intrinsically low effective magnetostriction and when elastic modulus and interfacial adhesion at heterogeneous interfaces are carefully controlled. In this aspect, using first-principles calculations, micromagnetic simulations, and finite-element mechanics within unified multiscale frameworks will enable quantitative prediction of strain-dependent magnetic responses across length scales. Coupling these physics-based models with deep learning and data-driven optimization can further accelerate the discovery of low-magnetostriction alloys and the design of strain-decoupled architectures, ultimately guiding predictive and adaptive development of flexible spintronic sensors. In addition to compositional control of FM materials, implementing AFM materials with compensated magnetic moments and ultrafast spin dynamics can further benefit from mechanical strain isolation, which stabilizes the exchange bias and anisotropy fields during integration on compliant substrates[50,51]. On the other hand, by enhancing other anisotropy contributions—such as magnetocrystalline, shape, and interfacial exchange anisotropies—which effectively dilutes the relative influence of the magnetoelastic term[166] and thereby stabilizes magnetization under strain[167,168]. Beyond optimizing material and interfacial properties, further opportunities arise from reconfigurable device geometries[169]. Designs such as kirigami-inspired patterns[8] or rolled-up configurations[19,47] transform conventional 2D stacks into compact 3D architectures, enabling simultaneous detection of in-plane and out-of-plane magnetic components without sacrificing fabrication simplicity or integration compatibility. Sustained performance under mechanical and environmental variation requires devices that are miniaturized, compliant, and geometrically adaptable. As summarized in Fig. 8, advances in curvilinear and shapeable spintronics, on-device signal conditioning, and transfer technologies are now aligning to address these issues toward flexible spintronic sensors that deliver selective and stable responses under continuous multiaxial deformation. Yet, open challenges remain, especially in suppressing progressive baseline drift under cyclic deformation—which undermines long-term signal fidelity—and in achieving reliable 3D field resolution in highly deformable devices. In particular, deformable spintronic sensors have shown that, under large out-of-plane deformation, the magnetic layer can tilt with respect to the external field, leading to angular misalignment and signal distortion. This tilting effect degrades field-direction accuracy and causes amplitude drift during multidirectional deformation. Overcoming this limitation will require co-design of mechanical structures and magnetic functionality. Symmetric stacking and positioning of active sensing layers can suppress curvature-induced tilt. In parallel, calibration and algorithmic correction including direction-cosine compensation and real-time vector reconstruction may restore true field alignment during complex motion. These approaches collectively point toward deformable spintronic platforms capable of maintaining vector accuracy and signal fidelity even under large, three-dimensional deformations. Progress along these directions will broaden the application spectrum of flexible spintronic sensors. In e-skin[9] and wearable systems[39], strain-decoupled magnetic sensor arrays enable vector-resolved magnetic mapping for gesture recognition and proprioception on compliant surfaces. In implantable platforms[21], mechanically adaptive magnetic sensors integrated on biocompatible materials demonstrate the potential for stable signal fidelity under physiological motion, supporting wireless cardiac and neural monitoring. Furthermore, magnetically guided microrobots and reconfigurable actuators rely on strain-insensitive magnetoresistive feedback for precise real-time control[9]. Consequently, these advances highlight the versatility of strain-decoupled spintronic sensors as conformable, miniaturized, and intelligent building blocks for next-generation soft-electronic architectures, enabling the development of environmentally adaptive electronics and autonomous micromachines.

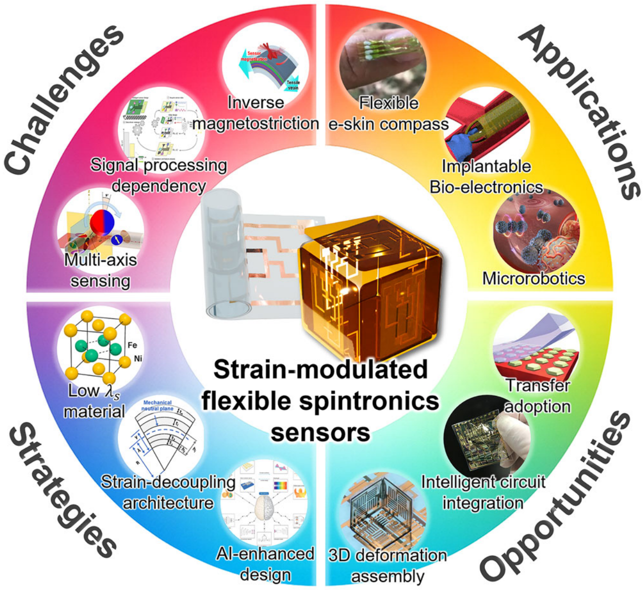

Fig. 8 | Outlook and future perspectives for strain-modulated flexible spintronic sensors. Flexible spintronic sensors open pathways to applications including electronic skin, implantable bioelectronics, and microrobotics, yet their performance remains constrained by strain sensitivity and fabrication limits. Advances in curvilinear and shapeable layouts, intelligent circuit integration, and transfer techniques provide routes toward devices with long-term stability under repeated deformation. Reproduced with permission from ref. 39 Copyright © 2018, Springer Nature[21]. Copyright © 2021, AAAS[193]. Copyright © 2022, American Chemical Society[165]. Copyright © 2006, Springer Nature[23]. Copyright © 2020, AAAS[8]. Copyright © 2022, Springer Nature[194]. Copyright © 2021, Springer Nature[169]. Copyright © 2019, AAAS, Copyright © 2021, Springer Nature[195].

Data availability

No datasets were generated or analyzed during the current study.

Received: 30 August 2025; Accepted: 18 November 2025;
Published online: 27 January 2026

References

1. Mostufa, S., Yari, P., Rezaei, B., Xu, K. & Wu, K. Flexible magnetic field nanosensors for wearable electronics: a review. *ACS Appl. Nano Mater.* **6**, 13732–13765 (2023).
2. Yang, H. et al. Advances in flexible magnetosensitive materials and devices for wearable electronics. *Adv. Mater.* **36**, 2311996 (2024).
3. Lugoda, P. et al. Submersible touchless interactivity in conformable textiles enabled by highly selective overbraided magnetoresistive sensors. *Commun. Eng.* **4**, 33 (2025).
4. Ge, J. et al. A bimodal soft electronic skin for tactile and touchless interaction in real time. *Nat. Commun.* **10**, 4405 (2019).
5. Makushko, P. et al. Flexible magnetoreceptor with tunable intrinsic logic for on-skin touchless human-machine interfaces. *Adv. Funct. Mater.* **31**, 2101089 (2021).
6. Liu, F. et al. Neuro-inspired electronic skin for robots. *Sci. Robot.* **7**, eabl7344 (2022).

7. Wang, Q. et al. Magnetostrictive bi-perceptive flexible sensor for tracking bend and position of human and robot hand. *Sci. Rep.* **14**, 20781 (2024).
8. Becker, C. et al. A new dimension for magnetosensitive e-skins: Active matrix integrated micro-origami sensor arrays. *Nat. Commun.* **13**, 2121 (2022).
9. Ha, M. et al. Reconfigurable magnetic origami actuators with on-board sensing for guided assembly. *Adv. Mater.* **33**, 2008751 (2021).
10. Yin, J., Wang, S., Tat, T. & Chen, J. Motion artefact management for soft bioelectronics. *Nat. Rev. Bioeng.* **2**, 541–558 (2024).
11. Park, B., Jeong, C., Ok, J. & Kim, T. -i Materials and structural designs toward motion artifact-free bioelectronics. *Chem. Rev.* **124**, 6148–6197 (2024).
12. Melzer, M. et al. Imperceptible magnetoelectronics. *Nat. Commun.* **6**, 6080 (2015).
13. Hu, H. et al. Large-area magnetic skin for multi-point and multi-scale tactile sensing with super-resolution. *npj Flex. Electron.* **8**, 42 (2024).
14. Dai, H. et al. Split-type magnetic soft tactile sensor with 3D force decoupling. *Adv. Mater.* **36**, 2310145 (2024).
15. Bandyopadhyay, S. Perspective: There is plenty of room for magnetic straintronics in the analog domain. *npj Spintronics* **2**, 15 (2024).
16. Kwon, H., Yang, Y., Kim, G., Gim, D. & Ha, M. Anisotropy in magnetic materials for sensors and actuators in soft robotic systems. *Nanoscale* **16**, 6778–6819 (2024).
17. Mostufa, S., Liang, S., Chugh, V. K., Wang, J.-P. & Wu, K. Spintronic devices for biomedical applications. *npj Spintronics* **2**, 26 (2024).
18. Wang, Z. et al. Highly sensitive flexible magnetic sensor based on anisotropic magnetoresistance effect. *Adv. Mater.* **28**, 9370–9377 (2016).
19. Singh, B. et al. Self-assembly as a tool to study microscale curvature and strain-dependent magnetic properties. *npj Flex. Electron.* **6**, 76 (2022).
20. Oliveros Mata, E. S. et al. Printable anisotropic magnetoresistance sensors for highly compliant electronics. *Appl. Phys. A* **127**, 280 (2021).
21. Rivkin, B. et al. Electronically integrated microcatheters based on self-assembling polymer films. *Sci. Adv.* **7**, eabl5408 (2021).
22. Ha, M. et al. Printable and stretchable giant magnetoresistive sensors for highly compliant and skin-conformal electronics. *Adv. Mater.* **33**, 2005521 (2021).
23. Kondo, M. et al. Imperceptible magnetic sensor matrix system integrated with organic driver and amplifier circuits. *Sci. Adv.* **6**, eaay6094 (2020).
24. Zhang, J., Jin, Z., Chen, G. & Chen, J. An ultrathin, rapidly fabricated, flexible giant magnetoresistive electronic skin. *Microsyst. Nanoeng.* **10**, 109 (2024).
25. Karnaushenko, D., Makarov, D., Yan, C., Streubel, R. & Schmidt, O. G. Printable giant magnetoresistive devices. *Adv. Mater.* **24**, 4518–4522 (2012).
26. Kim, S. N., Choi, J. W. & Lim, S. H. Tailoring of magnetic properties of giant magnetoresistance spin valves *via* insertion of ultrathin non-magnetic spacers between pinned and pinning layers. *Sci. Rep.* **9**, 1617 (2019).
27. Wu, K. et al. Giant magnetoresistance biosensors in biomedical applications. *ACS Appl. Mater. interfaces* **14**, 9945–9969 (2022).
28. Ota, S., Ando, A. & Chiba, D. A flexible giant magnetoresistive device for sensing strain direction. *Nat. Electron.* **1**, 124–129 (2018).
29. Makushko, P. et al. Scalable magnetoreceptive e-skin for energy-efficient high-resolution interaction towards undisturbed extended reality. *Nat. Commun.* **16**, 1647 (2025).
30. Chen, J.-Y., Lau, Y.-C., Coey, J., Li, M. & Wang, J.-P. High performance MgO-barrier magnetic tunnel junctions for flexible and wearable spintronic applications. *Sci. Rep.* **7**, 42001 (2017).
31. Ota, S., Ando, A., Sekitani, T., Koyama, T. & Chiba, D. Flexible CoFeB/MgO-based magnetic tunnel junctions annealed at high temperature (≥350 °C). *Appl. Phys. Lett.* **115** (2019).
32. Willing, S. et al. Novel tunnel magnetoresistive sensor functionalities *via* oblique-incidence deposition. *ACS Appl. Mater. interfaces* **13**, 32343–32351 (2021).
33. Melzer, M. et al. Wearable magnetic field sensors for flexible electronics. *Adv. Mater.* **27**, 1274–1280 (2015).
34. Granell, P. N. et al. Highly compliant planar Hall effect sensor with sub 200 nT sensitivity. *npj Flex. Electron.* **3**, 3 (2019).
35. Elzwawy, A. et al. Current trends in planar Hall effect sensors: evolution, optimization, and applications. *J. Phys. D: Appl. Phys.* **54**, 353002 (2021).
36. Jungwirth, T., Wunderlich, J. & Olejník, K. Spin Hall effect devices. *Nat. Mater.* **11**, 382–390 (2012).
37. Zhou, Y. et al. Giant magnetoelastic effect in soft systems for bioelectronics. *Nat. Mater.* **20**, 1670–1676 (2021).
38. Zhou, Y. et al. Theory of giant magnetoelastic effect in soft systems. *Sci. Adv.* **11**, eads0071 (2025).
39. Cañón Bermúdez, G. S. et al. Electronic-skin compasses for geomagnetic field-driven artificial magnetoreception and interactive electronics. *Nat. Electron.* **1**, 589–595 (2018).
40. Xu, R. et al. Self-healable printed magnetic field sensors using alternating magnetic fields. *Nat. Commun.* **13**, 6587 (2022).
41. Wang, C., Pan, C. & Wang, Z. Electronic skin for closed-loop systems. *ACS nano* **13**, 12287–12293 (2019).
42. Kong, D. et al. Direct observation of tensile-strain-induced nanoscale magnetic hardening. *Nat. Commun.* **14**, 3963 (2023).
43. Zhou, Y. et al. A multimodal magnetoelastic artificial skin for underwater haptic sensing. *Sci. Adv.* **10**, eadj8567 (2024).
44. Pradhan, G. et al. Magnetic properties of FeGa/Kapton for flexible electronics. *Sci. Rep.* **12**, 17503 (2022).
45. Liu, L. et al. Magnetostrictive GMR spin valves with composite FeGa/FeCo free layers. *AIP Adv.* **6** (2016).
46. Zhang, B., Lu, P., Tabrizian, R., Feng, P. X. L. & Wu, Y. 2D Magnetic heterostructures: spintronics and quantum future. *npj Spintronics* **2**, 6 (2024).
47. Fedorov, P. et al. Self-assembly of Co/Pt stripes with current-induced domain wall motion towards 3D racetrack devices. *Nat. Commun.* **15**, 2048 (2024).
48. Makarov, D. et al. New dimension in magnetism and superconductivity: 3d and curvilinear nanoarchitectures. *Adv. Mater.* **34**, 2101758 (2022).
49. Ji, G., Zhang, Y., Chai, Y. & Nan, T. Recent progress on controlling spin-orbit torques by materials design. *npj Spintronics* **2**, 56 (2024).
50. Liang, Y. et al. Field-free spin-orbit switching of perpendicular magnetization enabled by dislocation-induced in-plane symmetry breaking. *Nat. Commun.* **14**, 5458 (2023).
51. Yu, Z. et al. Field-Free Switching of Perpendicular Magnetization in Low-Symmetry Materials. *Adv. Funct. Mater.* 2505170 (2025).
52. Zhang, R. et al. Near-zero magnetostriction in magnetostrictive FeCo alloys. *Scr. Materialia* **203**, 114043 (2021).
53. Szymczak, H. From almost zero magnetostriction to giant magnetostrictive effects: recent results. *J. Magn. Magn. Mater.* **200**, 425–438 (1999).
54. Luzar, J. et al. Zero-magnetostriction magnetically soft high-entropy alloys in the $AlCoFeNiCu_x$ (x= 0.6–3.0) system for supersilent Applications. *Adv. Mater. Interfaces* **9**, 2201535 (2022).
55. Cho, C. et al. Strain-resilient electrical functionality in thin-film metal electrodes using two-dimensional interlayers. *Nat. Electron.* **4**, 126–133 (2021).
56. Callen, E. Magnetostriction. *J. Appl. Phys.* **39**, 519–527 (1968).
57. Khomskii, D. I. & Streltsov, S. V. Orbital effects in solids: Basics, recent progress, and opportunities. *Chem. Rev.* **121**, 2992–3030 (2020).

58. Stevens, K. W. H. The theory of paramagnetic relaxation. *Rep. Prog. Phys.* **30**, 189 (1967).
59. Coey, J. M. D. & Parkin, S. S. P. *Handbook of Magnetism and Magnetic Materials* (Springer International Publishing, 2021).
60. O'handley, R. C. Modern magnetic materials-principles and applications. *IEEE Electr. Insulation Mag.* **21**, 57–58 (2005).
61. Kong, D. et al. Strain engineering of magnetic anisotropy in the kagome magnet Fe3Sn2. *ACS Nano* **19**, 8142–8151 (2025).
62. Matsumoto, H., Ota, S., Ando, A. & Chiba, D. A flexible exchange-biased spin valve for sensing strain direction. *Appl. Phys. Lett.* **114** (2019).
63. Kwon, J.-H., Kwak, W.-Y. & Cho, B. K. Magnetization manipulation of a flexible magnetic sensor by controlled stress application. *Sci. Rep.* **8**, 15765 (2018).
64. Brown, W. F. Jr Theory of magnetoelastic effects in ferromagnetism. *J. Appl. Phys.* **36**, 994–1000 (1965).
65. Gambardella, P. et al. Giant magnetic anisotropy of single cobalt atoms and nanoparticles. *Science* **300**, 1130–1133 (2003).
66. Bruno, P. Tight-binding approach to the orbital magnetic moment and magnetocrystalline anisotropy of transition-metal monolayers. *Phys. Rev. B* **39**, 865 (1989).
67. Fan, X. et al. Magnetic field-dependent shape anisotropy in small patterned films studied using rotating magnetoresistance. *Sci. Rep.* **5**, 16139 (2015).
68. Prozorov, R. & Kogan, V. G. Effective demagnetizing factors of diamagnetic samples of various shapes. *Phys. Rev. Appl.* **10**, 014030 (2018).
69. Nogués, J. & Schuller, I. K. Exchange bias. *J. Magn. Magn. Mater.* **192**, 203–232 (1999).
70. Berkowitz, A. & Takano, K. Exchange anisotropy—a review. *J. Magn. Magn. Mater.* **200**, 552–570 (1999).
71. Chikazumi, S. & Graham, C. D. *Physics of ferromagnetism* (Oxford University Press, 1997).
72. Tannous, C. & Gieraltowski, J. The Stoner–Wohlfarth model of ferromagnetism. *Eur. J. Phys.* **29**, 475 (2008).
73. Amiri, M. S. et al. On the role of crystal and stress anisotropy in magnetic Barkhausen noise. *J. Magn. Magn. Mater.* **372**, 16–22 (2014).
74. Cullity, B. D. & Graham, C. D. *Introduction to Magnetic Materials* (John Wiley & Sons, 2011).
75. Kittel, C. Physical theory of ferromagnetic domains. *Rev. Mod. Phys.* **21**, 541 (1949).
76. Sander, D. The correlation between mechanical stress and magnetic anisotropy inultrathin films. *Rep. Prog. Phys.* **62**, 809 (1999).
77. Berger, L. Magnetostriction in nickel alloys. *Phys. Rev.* **138**, A1083 (1965).
78. Berger, L. Influence of spin-orbit interaction on the transport processes in ferromagnetic nickel alloys, in the presence of a degeneracy of the 3d band. *Physica* **30**, 1141–1159 (1964).
79. Kim, C., Kim, B.-H. & Min, B. Magnetostriction in antiferromagnetic systems. *J. Korean Magn. Soc.* **18**, 159–162 (2008).
80. Lüthi, B. Crystal field effects in rare earth systems. *J. Magn. Magn. Mater.* **15**, 1–8 (1980).
81. Andriessen, J., Van Der Kolk, E. & Dorenbos, P. Lattice relaxation study of the 4f-5d excitation of Ce^{3+}-doped La Cl$_3$, LaBr$_3$, and NaLaF$_4$: Stokes shift by pseudo Jahn-Teller effect. *Phys. Rev. B—Condens. Matter Mater. Phys.* **76**, 075124 (2007).
82. Jensen, J. & Mackintosh, A. R. *Rare Earth Magnetism: Structures and Excitations* (Oxford University Press, 1991).
83. Schmitt, D. Angular distribution of 4f electrons in the presence of a crystal field. *J. Phys.* **47**, 677–681 (1986).
84. Iwamoto, T., Mito, M., Hidaka, M., Kawae, T. & Takeda, K. Magnetic measurement of rare earth ferromagnet gadolinium under high pressure. *Phys. B: Condens. Matter* **329**, 667–668 (2003).
85. Ryan, P. et al. Multiferroic behavior in EuTiO$_3$ films constrained by symmetry. *Phys. Rev. B* **101**, 180409 (2020).
86. Doerr, M., Rotter, M. & Lindbaum, A. Magnetostriction in rare-earth based antiferromagnets. *Adv. Phys.* **54**, 1–66 (2005).
87. Tang, N. et al. Crystal field magnetostriction of spin ice under ultrahigh magnetic fields. *Phys. Rev. B* **110**, 214414 (2024).
88. White, J. S. et al. Strain-induced ferromagnetism in antiferromagnetic LuMnO$_3$ thin films. *Physical Review Letters* **111** (2013).
89. Widyandaru, H. Y. & Gohda, Y. Tunable magnetic coupling of monolayer CrI$_2$ by strain engineering. *npj Spintronics* **3** (2025).
90. Cenker, J. et al. Reversible strain-induced magnetic phase transition in a van der Waals magnet. *Nat. Nanotechnol.* **17**, 256–261 (2022).
91. Zollner, K., Kurpas, M., Gmitra, M. & Fabian, J. First-principles determination of spin–orbit coupling parameters in two-dimensional materials. *Nat. Rev. Phys.* **7**, 255–269 (2025).
92. Hu, S. et al. Strain-enhanced spin-orbit coupling in permalloy thin films. *Phys. Rev. B* **109**, 224407 (2024).
93. Wang, Y. et al. Strain-Sensitive Magnetization Reversal of a van der Waals Magnet. *Adv. Mater.* **32**, 2004533 (2020).
94. Shao, Y. C. et al. Strain effect on orbital and magnetic structures of Mn ions in epitaxial Nd $_{0.35}$Sr$_{0.65}$MnO$_3$/SrTiO$_3$ films using X-ray diffraction and absorption. *Sci. Rep.* **9** (2019).
95. Ko, E. K. et al. Tuning orbital-selective phase transitions in a two-dimensional Hund's correlated system. *Nat. Commun.* **14**, 3572 (2023).
96. Fernandez, A. et al. Strain-Induced Orbital Contributions to Oxygen Electrocatalysis in Transition-Metal Perovskites. *Adv. Energy Mater.* **11**, 2102175 (2021).
97. Biało, I. et al. Strain-tuned incompatible magnetic exchange-interaction in La$_2$NiO$_4$. *Commun. Phys.* **7** (2024).
98. Bi, X., Qiu, C., Qin, F., Huang, J. & Yuan, H. Controlling exchange interactions and emergent magnetic phenomena in layered 3*d*-orbital ferromagnets. *Adv. Phys. Res.* **2**, 2200106 (2023).
99. Deng, L. et al. Writing and reading magnetization states *via* strain in Fe3GaTe2/*h*-BN/MnBi$_2$Te$_4$ junction. *J. Appl. Phys.* **135** (2024).
100. Wu, R., Chen, L., Shick, A. & Freeman, A. First-principles determinations of magneto-crystalline anisotropy and magnetostriction in bulk and thin-film transition metals. *J. Magn. Magn. Mater.* **177**, 1216–1219 (1998).
101. Klokholm, E. & Aboaf, J. The saturation magnetostriction of permalloy films. *J. Appl. Phys.* **52**, 2474–2476 (1981).
102. McKeehan, L. & Cioffi, P. Magnetostriction in permalloy. *Phys. Rev.* **28**, 146 (1926).
103. Kim, Y. & Silva, T. J. Magnetostriction characteristics of ultrathin permalloy films. *Appl. Phys. Lett.* **68**, 2885–2886 (1996).
104. Kawai, T., Ouchi, S., Ohtake, M. & Futamoto, M. Thickness Effect on Magnetostriction of Fe and Fe$_{98}$B$_2$ Thin Films. *IEEE Trans. Magn.* **48**, 1585–1588 (2012).
105. Den Broeder, F., Hoving, W. & Bloemen, P. Magnetic anisotropy of multilayers. *J. Magn. Magn. Mater.* **93**, 562–570 (1991).
106. Ohldag, H., Shi, H., Arenholz, E., Stöhr, J. & Lederman, D. Parallel versus antiparallel interfacial coupling in exchange biased Co/FeF$_2$. *Phys. Rev. Lett.* **96**, 027203 (2006).
107. Sahoo, A. K. et al. Spin pumping in magnetostrictive Galfenol interfaced with Ta. *Adv. Funct. Mater.* 2424006 (2025).
108. Chen, Z. et al. Complex strain evolution of polar and magnetic order in multiferroic BiFeO$_3$ thin films. *Nat. Commun.* **9**, 3764 (2018).
109. Koohfar, S. et al. Effect of strain on magnetic and orbital ordering of LaSrCrO$_3$/LaSrMnO$_3$ heterostructures. *Phys. Rev. B* **101**, 064420 (2020).
110. Herzer, G. Grain size dependence of coercivity and permeability in nanocrystalline ferromagnets. *IEEE Trans. Magn.* **26**, 1397–1402 (1990).

111. Guerra, Y., Peña-Garcia, R. & Padrón-Hernández, E. Magnetic reversion in real nickel and cobalt nanowires and the angular dependence of coercivity. *J. Magn. Magn. Mater.* **452**, 17–22 (2018).
112. Guerra, Y., Peña-Garcia, R. & Padrón-Hernández, E. Dipolar magnetic interaction effects in 2D hexagonal array of cobalt hollow-spheres. *J. Magn. Magn. Mater.* **451**, 269–275 (2018).
113. Wang, J. et al. Magnetic domain wall engineering in a nanoscale permalloy junction. *Appl. Phys. Lett.* **111** (2017).
114. Agudelo-Giraldo, J. D., Restrepo-Parra, E. & Restrepo, J. Grain boundary anisotropy on nano-polycrystalline magnetic thin films. *Sci. Rep.* **10**, 5041 (2020).
115. Li, H. & Tonner, B. Direct experimental identification of the structure of ultrathin films of bcc iron and metastable bcc and fcc cobalt. *Phys. Rev. B* **40**, 10241 (1989).
116. Fukunaga, H. F. H. & Inoue, H. I. H. Effect of intergrain exchange interaction on magnetic properties in isotropic Nd-Fe-B magnets. *Jpn. J. Appl. Phys.* **31**, 1347 (1992).
117. Twarowski, K., Kuźmiński, M., lawska-Waniewska, A., Lachowicz, H. & Herzer, G. Magnetostriction and its temperature dependence in FeCuNbSiB nanocrystalline alloy. *J. Magn. Magn. Mater.* **150**, 85–92 (1995).
118. Ślawska-Waniewska, A., Żuberek, R. & Nowicki, P. Saturation magnetostriction of FeZrB (Cu) nanocrystalline alloys. *J. Magn. Magn. Mater.* **157**, 147–148 (1996).
119. Szymczak, H. & Żuberek, R. Surface magnetostriction. *Acta Phys. Polonica A* **83**, 651–659 (1993).
120. Dang, P. et al. Ultrahigh elastic energy storage in nanocrystalline alloys with martensite nanodomains. *Adv. Mater.* **36**, 2408275 (2024).
121. Liu, D. et al. Strain analysis and engineering in halide perovskite photovoltaics. *Nat. Mater.* **20**, 1337–1346 (2021).
122. Moridi, A., Ruan, H., Zhang, L. & Liu, M. Residual stresses in thin film systems: effects of lattice mismatch, thermal mismatch and interface dislocations. *Int. J. Solids Struct.* **50**, 3562–3569 (2013).
123. Shin, Y. et al. Damage-free dry transfer method using stress engineering for high-performance flexible two-and three-dimensional electronics. *Nat. Mater.* **23**, 1411–1420 (2024).
124. Long, H. et al. Effect of lattice misfit on the evolution of the dislocation structure in Ni-based single crystal superalloys during thermal exposure. *Acta Materialia* **120**, 95–107 (2016).
125. Emori, K. et al. Surface buckling delamination patterns of film on soft spherical substrates. *Soft Matter* **16**, 3952–3961 (2020).
126. Kuhr, B., Farkas, D., Robertson, I. M., Johnson, D. & Was, G. Stress localization resulting from grain boundary dislocation interactions in relaxed and defective grain boundaries. *Metall. Mater. Trans. A* **51**, 667–683 (2020).
127. Hua, Q. et al. Skin-inspired highly stretchable and conformable matrix networks for multifunctional sensing. *Nat. Commun.* **9**, 244 (2018).
128. Injeti, S.S. & Annabattula, R. K. Extending Stoney's equation to thin, elastically anisotropic substrates and bilayer films. *Thin Solid Films* **598**, 252-259 (2016).
129. Kim, D. H., Xiao, J., Song, J., Huang, Y. & Rogers, J. A. Stretchable, curvilinear electronics based on inorganic materials. *Adv. Mater.* **22**, 2108–2124 (2010).
130. Yang, Y., Winkler, A. & Karimzadeh, A. A practical approach for determination of thermal stress and temperature-dependent material properties in multilayered thin films. *ACS Appl. Mater. Interfaces* **16**, 31729–31737 (2024).
131. Yosida, K. Magnetic properties of Cu-Mn alloys. *Phys. Rev.* **106**, 893 (1957).
132. Ruderman, M. A. & Kittel, C. Indirect exchange coupling of nuclear magnetic moments by conduction electrons. *Phys. Rev.* **96**, 99 (1954).
133. Kasuya, T. A theory of metallic ferro-and antiferromagnetism on Zener's model. *Prog. Theor. Phys.* **16**, 45–57 (1956).
134. Zhou, L. et al. Strength and directionality of surface Ruderman–Kittel–Kasuya–Yosida interaction mapped on the atomic scale. *Nat. Phys.* **6**, 187–191 (2010).
135. Chen, Y. -f et al. Towards flexible magnetoelectronics: buffer-enhanced and mechanically tunable GMR of Co/Cu multilayers on plastic substrates. *Adv. Mater.* **20**, 3224–3228 (2008).
136. Schrag, B. et al. Néel "orange-peel" coupling in magnetic tunneling junction devices. *Appl. Phys. Lett.* **77**, 2373–2375 (2000).
137. Sidles, J. A., Garbini, J. L., Dougherty, W. M. & Shih-Hui, C. The classical and quantum theory of thermal magnetic noise, with applications in spintronics and quantum microscopy. *Proc. IEEE* **91**, 799–816 (2003).
138. Wittrock, S. et al. Low offset frequency 1/f flicker noise in spin-torque vortex oscillators. *Phys. Rev. B* **99**, 235135 (2019).
139. Jantsch, O. Flicker (1/f) noise generated by a random walk of electrons in interfaces. *IEEE Trans. electron devices* **34**, 1100–1115 (2005).
140. Larocque, S., Pinsolle, E., Lupien, C. & Reulet, B. Shot noise of a temperature-biased tunnel junction. *Phys. Rev. Lett.* **125**, 106801 (2020).
141. Herranen, T. & Laurson, L. Barkhausen noise from precessional domain wall motion. *Phys. Rev. Lett.* **122**, 117205 (2019).
142. Abdallh, A. A.-E. & Dupré, L. Local magnetic measurements in magnetic circuits with highly non-uniform electromagnetic fields. *Meas. Sci. Technol.* **21**, 045109 (2010).
143. Fadil, D. et al. Direct observation of magnetization reversal and low field magnetoresistance of epitaxial $La_{0.7}Sr_{0.3}MnO_3/SrTiO_3$ (001) thin films at room temperature. *J. Appl. Phys.* **112** (2012).
144. Raghunath, G., Marana, M., Na, S.-M. & Flatau, A. Kerr microscopy studies of the effects of bending stress on galfenol. *J. Appl. Phys.* **115** (2014).
145. Kang, D. et al. Ultrasensitive mechanical crack-based sensor inspired by the spider sensory system. *Nature* **516**, 222–226 (2014).
146. Zhao, Z. et al. Failure mechanisms in flexible electronics. *Int. J. Smart Nano Mater.* **14**, 510–565 (2023).
147. Huo, Y. et al. Low noise, strain modulated, multiferroic magnetic field sensor systems. *IEEE Sens. J.* **23**, 14025–14040 (2023).
148. Han, K., Huang, Q., Ong, P. & Ong, C. Low-frequency noise in $La_{0.7}Sr_{0.\ 3}Mn_{1-x}Fe_xO_3$ thin films. *J. Phys.: Condens. Matter* **14**, 6619 (2002).
149. Kalita, V. M. & Ryabchenko, S. M. Equilibrium magnetization of a nanogranular magnetic film with perpendicular anisotropy in a tilted magnetic field. *Low. Temp. Phys.* **38**, 199–205 (2012).
150. Pan, L. et al. Flexible Magnetic Sensors. *Sensors* **23**, 4083 (2023).
151. Li, B., Kavaldzhiev, M. N. & Kosel, J. Flexible magnetoimpedance sensor. *J. Magn. Magn. Mater.* **378**, 499–505 (2015).
152. Tyagi, A., Martini, L., Gebeyehu, Z. M., Mišeikis, V. & Coletti, C. Highly sensitive Hall sensors based on chemical vapor deposition graphene. *ACS Appl. Nano Mater.* **7**, 18329–18336 (2024).
153. Lin, G. et al. A highly flexible and compact magnetoresistive analytic device. *Lab Chip* **14**, 4050–4058 (2014).
154. Spetzler, E., Spetzler, B. & McCord, J. A magnetoelastic twist on magnetic noise: the connection with intrinsic nonlinearities. *Adv. Funct. Mater.* **34**, 2309867 (2024).
155. Chung, J. Y., Nolte, A. J. & Stafford, C. M. Surface wrinkling: a versatile platform for measuring thin-film properties. *Adv. Mater.* **23**, 349–368 (2011).
156. Xu, S. et al. Soft microfluidic assemblies of sensors, circuits, and radios for the skin. *Science* **344**, 70–74 (2014).
157. Kim, D.-H. et al. Materials and noncoplanar mesh designs for integrated circuits with linear elastic responses to extreme

mechanical deformations. *Proc. Natl. Acad. Sci.* **105**, 18675–18680 (2008).
158. Wu, G.-W., Hsiue, G.-H. & Yang, J.-S. Stress relaxation in poly (styrene-butadiene-styrene) and poly (styreneisoprene-styrene) triblock copolymers and their derivatives. *Mater. Chem. Phys.* **37**, 191–196 (1994).
159. Eshelby, J. D. The determination of the elastic field of an ellipsoidal inclusion, and related problems. *Proc. R. Soc. Lond. Ser. A: Math. Phys. Sci.* **241**, 376–396 (1957).
160. Yao, K. & Zhuang, Q. Self-decoupling three-axis forces in a simple sensor. *Nat. Mach. Intell.* **6**, 1431–1432 (2024).
161. Liao, Y., Cao, J., Yu, L., Xiang, J. & Zhao, Y. A multi-sensor gait dataset collected under non-standardized dual-task conditions. *Sci. data* **12**, 1121 (2025).
162. Kong, D. et al. Super-resolution tactile sensor arrays with sparse units enabled by deep learning. *Sci. Adv.* **11**, eadv2124 (2025).
163. He, L. et al. Machine learning assisted intelligent design of meta structures: a review. *Microstructures* **3**, N/A-N/A (2023).
164. Kang, J.-H. et al. Monolithic 3D integration of 2D materials-based electronics towards ultimate edge computing solutions. *Nat. Mater.* **22**, 1470–1477 (2023).
165. Meitl, M. A. et al. Transfer printing by kinetic control of adhesion to an elastomeric stamp. *Nat. Mater.* **5**, 33–38 (2006).
166. Qiao, X. et al. Enhanced stress-invariance of magnetization direction in magnetic thin films. *Appl. Phys. Lett.* **111** (2017).
167. Bao, X. et al. Flexible exchange-biased films with superior strain stability. *Adv. Funct. Mater.* **34**, 2409844 (2024).
168. Li, M. et al. Enhanced stress stability in flexible Co/Pt multilayers with strong perpendicular magnetic anisotropy. *Nano Lett.* **23**, 8073–8080 (2023).
169. Becker, C. et al. Self-assembly of highly sensitive 3D magnetic field vector angular encoders. *Sci. Adv.* **5**, eaay7459 (2019).
170. Wu, H. et al. Strategy for co-enhancement of interface adhesion and coercivity of Nd-Fe-B grain boundary diffusion magnet: TbH_3 nanopowders used in screen printing. *J. Magn. Magn. Mater.* **610**, 172595 (2024).
171. Vas, J. V. et al. Direct visualization of local magnetic domain dynamics in a 2D Van der Walls material/ferromagnet interface. *Commun. Phys.* **7**, 407 (2024).
172. Dagge, K., Frank, W., Seeger, A. & Stoll, H. 1/f noise as an early indicator of electromigration damage in thin metal films. *Appl. Phys. Lett.* **68**, 1198–1200 (1996).
173. Zhang, X. et al. Effect of buffer layer and external stress on magnetic properties of flexible FeGa films. *J. Appl. Phys.* **113** (2013).
174. Mittal, K. The role of the interface in adhesion phenomena. *Polym. Eng. Sci.* **17**, 467–473 (1977).
175. Li, Y. et al. Achieving tissue-level softness on stretchable electronics through a generalizable soft interlayer design. *Nat. Commun.* **14**, 4488 (2023).
176. Parks, D., Chen, P., Egelhoff, W. & Gomez, R. D. Interfacial roughness effects on interlayer coupling in spin valves grown on different seed layers. *J. Appl. Phys.* **87**, 3023–3026 (2000).
177. Fleischmann, C. et al. The influence of interface roughness on the magnetic properties of exchange biased CoO/Fe thin films. *J. Appl. Phys.* **107** (2010).
178. Ni, D. & Christofides, P. D. Dynamics and control of thin film surface microstructure in a complex deposition process. *Chem. Eng. Sci.* **60**, 1603–1617 (2005).
179. Kuch, W. et al. Tuning the magnetic coupling across ultrathin antiferromagnetic films by controlling atomic-scale roughness. *Nat. Mater.* **5**, 128–133 (2006).
180. Yamaura, S., Furuya, Y. & Watanabe, T. The effect of grain boundary microstructure on Barkhausen noise in ferromagnetic materials. *Acta Materialia* **49**, 3019–3027 (2001).
181. Schrefl, T., Schmidts, H., Fidler, J. & Kronmüller, H. Nucleation of reversed domains at grain boundaries. *J. Appl. Phys.* **73**, 6510–6512 (1993).
182. Lee, S.-L. & Richards, N. Influence of long term annealing on grain boundary character distributions in nickel. *Mater. Sci. Eng.: A* **405**, 74–85 (2005).
183. Li, Q. & Teng, Y. Distribution of grain boundary plane orientation texture in hot deformed Nd-Fe-B magnets and its texture enhancement mechanism. *J. Alloys. Compounds* 181692 (2025).
184. Lisfi, A. et al. Reorientation of magnetic anisotropy in epitaxial cobalt ferrite thin films. *Phys. Rev. B—Condens. Matter Mater. Phys.* **76**, 054405 (2007).
185. Schwienbacher, D. et al. Magnetoelasticity of $Co_{25}Fe_{75}$ thin films. *J. Appl. Phys.* **126** (2019).
186. Takahashi, R., Misumi, H. & Lippmaa, M. Self-template growth of orientation-controlled Fe3O4 thin films. *Cryst. Growth Des.* **12**, 2679–2683 (2012).
187. Cheng, F. et al. Chemical synthesis and magnetic study of nanocrystalline thin films of cobalt spinel ferrites. *Solid State Commun.* **107**, 471–476 (1998).
188. Barturen, M. et al. Bulklike behavior of magnetoelasticity in epitaxial $Fe_{1-x}Ga_x$ thin films. *Phys. Rev. B* **99**, 134432 (2019).
189. Aristov, D. Indirect RKKY interaction in any dimensionality. *Phys. Rev. B* **55**, 8064 (1997).
190. Toney, M. F., Samant, M. G., Lin, T. & Mauri, D. Thickness dependence of exchange bias and structure in MnPt and MnNi spin valves. *Appl. Phys. Lett.* **81**, 4565–4567 (2002).
191. Hong, J. E. et al. Strain-insensitive ferromagnetic $SrRuO_3$ thin films with ferrimagnetic CoFe2O4 buffer layer. *Curr. Appl. Phys.* **66**, 24–29 (2024).
192. Hunter, D. et al. Giant magnetostriction in annealed $Co_{1-x}Fe_x$ thin-films. *Nat. Commun.* **2**, 518 (2011).
193. Gong, D., Celi, N., Zhang, D. & Cai, J. Magnetic biohybrid microrobot multimers based on chlorella cells for enhanced targeted drug delivery. *ACS Appl. Mater. interfaces* **14**, 6320–6330 (2022).
194. Ballard, Z., Brown, C., Madni, A. M. & Ozcan, A. Machine learning and computation-enabled intelligent sensor design. *Nat. Mach. Intell.* **3**, 556–565 (2021).
195. Ma, W. et al. Deep learning for the design of photonic structures. *Nat. Photonics* **15**, 77–90 (2021).

Acknowledgements

The authors thank K. S. Lee for valuable comments and discussions. This work was supported by the National Research Foundation of Korea (NRF) grants funded by the Korea government (MIST) (RS-2025-25442536, 2022R1C1C1004845).

Author contributions

M.O. wrote the main manuscript text and prepared the figures. Y.K. assisted with figure preparation. M.H. supervised the overall study as corresponding author and contributed to the conception, writing, and editing of the manuscript. All authors reviewed the manuscript.

Competing interests

The authors declare no competing interests.

Additional information

Correspondence and requests for materials should be addressed to Minjeong Ha.